Applied Energy 360 (2024) 122697

Contents lists available at ScienceDirect

Applied Energy

journal homepage: www.elsevier.com/locate/apenergy

An effective predictor of the dynamic operation of latent heat thermal energy storage units based on a non-linear autoregressive network with exogenous inputs

Pranaynil Saikia *, Héctor Bastida, Carlos E. Ugalde-Loo

School of Engineering, Cardiff University, Wales, UK

HIGHLIGHTS

- The state of a TES unit is continuously quantified with a non-intrusive NARX model.
- The NARX model trained on physics-based data replicates the real system's response.
- Heating zone-wise segregation of prediction tasks boosts the model's accuracy.
- The NARX model is 86% faster than a physics-based model built for fast computation.
- Limited public availability of a NARX model is addressed by code and data sharing.

GRAPHICAL ABSTRACT

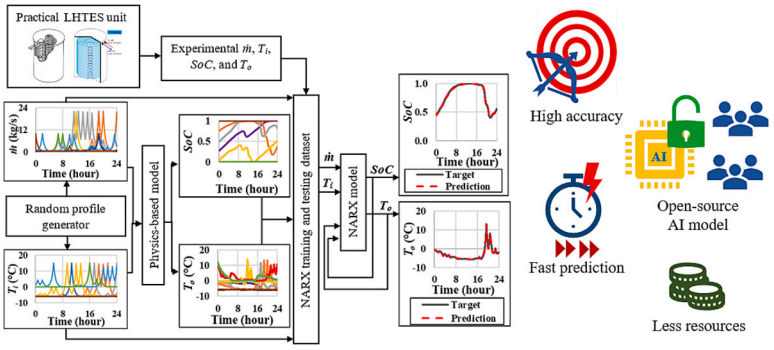

ARTICLE INFO

Keywords:
Latent heat thermal energy storage systems
Artificial intelligence
Thermal networks
State-of-charge estimator
Open-source
Non-linear autoregressive network with exogenous inputs

ABSTRACT

Thermal networks require thermal energy storage (TES) provisions for balancing thermal energy sources with variable consumer demand. Harvesting ice is an economical option for latent heat TES systems in cooling networks given the wide availability of the storage medium. This paper presents an artificial intelligence (AI) based model to monitor the state-of-charge (SoC) and the outlet temperature of the heat transfer fluid (T_o) of an ice tank under fluctuating operating conditions. The AI model is a non-linear autoregressive network with exogenous inputs (NARX) that was trained and tested with datasets obtained from experimental measurements of a practical ice tank and a physics-based model of the tank. The NARX model was sensitised with physics-informed attributes to recognise different heating and cooling zones. The model exhibits a high accuracy in predicting the operating conditions of the ice tank when benchmarked against both experimental measurements of a practical tank and outputs from the physics-based model. For instance, it achieves R^2 values of 0.9943 and 0.9842 for SoC and T_o, with root mean square errors of 1.73% for SoC and 0.3161°C for T_o. The NARX model is 86% faster than its physics-based counterpart and its implementation requires limited computational resources—making it suitable as a standalone estimator for the TES operation and the accelerated simulation of energy systems containing latent heat TES units. Furthermore, given the limited availability of NARX models in open-source libraries, the presented NARX model and relevant datasets have been made available alongside this paper to contribute to open-science in energy research and the broader AI community.

* Corresponding author.
E-mail address: SaikiaP@cardiff.ac.uk (P. Saikia).

https://doi.org/10.1016/j.apenergy.2024.122697
Received 17 August 2023; Received in revised form 22 December 2023; Accepted 18 January 2024
Available online 7 February 2024

Nomenclature and variables

Abbreviation

1-D	one-dimensional
3-D	three-dimensional
ANN	artificial neural network
HTF	heat transfer fluid
LHS	Latin hypercube sampling
LSTM	long short-term memory
LHTES	latent heat thermal energy storage
MCDM	multi-criteria decision-making
MCS	Monte-Carlo sampling
MSE	mean square error
NARX	non-linear autoregressive network with exogenous inputs
PCM	phase change material
R^2	determination coefficient
RMSE	root mean square error
RNN	recurrent neural network
SoC	state-of-charge
TES	thermal energy storage
TOPSIS	technique for order preference by similarity to ideal solution

A_c	cross-sectional area [m^2]
A_{ex}	surface area [m^2]
A_{tr}	heat transfer area [m^2]
A_w	cross-sectional area of ice [m^2]
D_t	tube hydraulic diameter [mm]
$\dot{E}$	rate of change of energy [W]
V_f	heat transfer fluid volume [m^3]
V_w	ice volume [m^3]
c_p	specific heat [J/(kg°C)]
k_t	thermal conductivity of tube [W/(m°C)]
k_w	water/ice thermal conductivity [W/(m°C)]
r_i	tube internal radius [mm]
r_o	tube external radius [mm]
r_w	ice radius [mm]
$\dot{m}$	mass flow rate of heat transfer fluid [kg/s]
T	temperature [°C]
T_i	inlet temperature of heat transfer fluid [°C]
T_o	outlet temperature of heat transfer fluid [°C]
L	tube length [m]
U	heat transfer coefficient [W/(m^2°C)]
ρ	density [kg/m^3]

1. Introduction

The global drive to incorporate renewable energy technologies to mitigate greenhouse gas emissions has prompted substantial developments in energy storage systems. Energy storage provision is suitable to overcome the intermittent availability of renewable energy sources (such as solar and wind) and to balance the temporal mismatch between energy demand and supply [1,2].

Heat is a major form of energy in both industrial and residential applications. Waste heat from industries is now increasingly recovered for possible co-generation purposes [3]. The use of solar thermal systems has also increased over recent years. These heat sources, which have intermittency inherently embedded into their functioning, can benefit from thermal energy storage (TES) devices for a better energy delivery and utilisation [4].

Sensible heat and latent heat energy storage are the main types of TES technologies. Latent heat TES (LHTES) systems exhibit a higher energy storage density when compared to sensible heat TES systems. This attribute helps in designing compact thermal stores for the load management in a thermal network when physical space is a constraint [5]. In an LHTES unit, a heat transfer fluid (HTF) is used to inject or release the thermal energy. A phase change material (PCM) acts as the storage medium. It releases or absorbs a large amount of thermal energy during a change in phase—occurring at isothermal conditions. Ice storage tanks operating in the water-ice phase transition regime are a commonly adopted latent heat-based option for cooling systems given their high energy density and the low cost of the storage medium [6].

To effectively monitor the performance of an LHTES system, its state-of-charge (SoC) needs to be assessed on a timely basis as the thermal store exchanges heat with other components within an energy system. The SoC of an LHTES unit represents how much of the total latent heat value of the storage medium has been released or absorbed. Thus, SoC indicates the level of availability of thermal energy at a given instant. An LHTES unit can be harnessed effectively for energy management if its charging and discharging operations are optimally scheduled, which in turn depend on the timely and accurate estimation of SoC [7].

Different approaches have been employed to model the thermal dynamics of LHTES units, from simple steady-state models to complex three-dimensional (3-D) finite element-based representations. In steady-state models, parameters such as heat transfer coefficients or the thermophysical properties of the PCM are often considered as constant [8,9]. Moreover, the use of algebraic equations to iteratively solve the model disregards the dynamic changes present during practical operating conditions [10]. Thus, accuracy of the simulation results is limited in general. In contrast, a highly accurate 3-D modelling approach uses conservation laws (energy, momentum, and mass) and the temperature-dependent thermophysical properties of the PCM and HTF to describe the internal dynamics of the system by employing partial differential equations. Such detailed modelling of the system behaviour requires high-performance computing and large simulation times to solve the models [11].

There are modelling methodologies in the middle of the aforementioned extremes where only one or two dimensions of the internal structure of the system are sufficient to accurately describe the thermal dynamics of the LHTES unit. Such methodologies represent plausible options to develop low-complexity models. In some cases, these approaches may still consider the temperature dependence of the thermophysical properties of the PCM and the dynamic calculation of the heat transfer coefficients. Consequently, a reduced computation time is required to run simulations compared to 3-D models.

For industrial energy storage applications, traditional methods for monitoring critical operating parameters have predominantly relied on a combination of manual inspections and sensor-based systems. Engineers and technicians have historically performed periodic physical checks on the storage units to assess component conditions, fluid levels, energy levels, and overall performance. In the case of TES systems, thermocouples and thermometers have been widely employed to measure temperature variations. Large hot water TES tanks often utilise multi-spot thermometers to gauge water temperature and estimate the level of thermal stratification [12]. The fluid flow rates associated with charging and discharging of TES units are commonly measured by differential pressure sensors [13]. To address leakages in hot water storage systems, detection methods range from simple visual inspections to the implementation of advanced leakage sensors for underground tanks where visual inspection is not feasible [12].

On the other hand, electrical batteries employ electronic sensors to measure current and voltage [14]. For more sophisticated monitoring, fibre Bragg grating sensors are utilised to estimate SoC by measuring temperature and strain in batteries during operation [15]. These sensors provide real-time data, allowing operators to identify any deviations

from expected values.

The conventional monitoring methods for energy storage systems described in the previous paragraphs often present limitations in terms of efficiency and accuracy. For instance, manual inspections may be infrequent, leading to potential delays in detecting issues, while sensor-based systems may be expensive. For a TES tank, although low-cost temperature sensors may be available to effectively measure the input and output temperature, a good quantification of SoC requires a precise knowledge of the temperature gradient of the storage medium. For vertical sensible heat hot water tanks, the common practical approach is to mount temperature sensors through the tank's height—exploiting thermal stratification within the unit. These sensors may not be expensive and SoC calculation is achieved using the temperature measurements and the specific heat capacity of water [16].

Nevertheless, accurately monitoring SoC within an LHTES unit requires information of not only the HTF, but also the PCM throughout the tank. Quantifying effectively the temperature gradient of the PCM may be challenging as it would require reliable and precise temperature measurements and this would only be achieved when several sensors are installed [17,18]. This is because the phase change of a PCM causes its total volume to temporarily fractionate into liquid and solid volumes irregularly distributed in the tank. In addition, incorporating several temperature sensors within the unit's enclosure may be disruptive as this would imply additional design considerations linked to the internal arrangement of the tubes carrying the HTF and the actual sensor location.

There are other simpler solutions deployed in practice for LHTES units, such as using pressure sensors to indirectly determine SoC. In such an approach, a relation between pressure changes and the change in the phase fraction of a PCM is established [19]. In case of an ice tank, a differential pressure transducer could be employed to measure the change in volume when ice is formed, but this could be affected by the presence of ice pockets or compression effects [20].

To avoid the challenging implementation of internal temperature sensors to accurately characterise the temperature gradient of a PCM and facilitate an effective quantification of SoC, temperature estimation thus represents a suitable approach requiring a limited amount of external sensors. Such estimation can be done with either physics-based models or data-driven models based on machine learning techniques and artificial intelligence (AI). Autoregressive AI-based models, in particular, can continuously determine the SoC of LHTES units by capitalising on their own estimates of outlet temperature prediction.

With the advent of AI and the development of data-driven models, the computation time of physics-based models for assessing the behaviour of an energy system can be further reduced. Such AI models have demonstrated the potential to replicate complex system behaviour with a high accuracy [21]. Feed-forward artificial neural networks (ANNs) offer a wide range of hyperparameters to tune AI models for accurate predictions. For instance, such ANNs have been used in [22] to predict, with a high accuracy, the heat absorbed and released by the PCM of an LHTES system during charging and discharging cycles when compared to experimentally measured values. In [23], a feed-forward back propagation ANN was used to estimate the thermal energy stored in an LHTES system. Time was used as an independent variable in addition to the heat transfer area, the Reynolds number, and the inlet temperature of the HTF for training the ANN on time-series data. This approach, however, has a caveat, given that the long-duration operation of the thermal store would require large values of time inputs to the ANN. The ANN, therefore, must be trained on a large dataset that covers up to the maximum time duration until which the LHTES unit may function. However, an LHTES unit can be integrated as an element of an energy system that functions indefinitely—thus leading to very large values of the time input variable.

Recurrent AI models such as recurrent neural networks (RNNs) can handle time-series data more efficiently. An RNN exploits information from the previous time-step by forming connections with its previous state of hidden neurons, thereby allowing data from previous inputs to influence the output for future time-steps. Underpinning the potential of RNNs in mapping time-series inputs and outputs, studies have been conducted in recent years to estimate the SoC of electrical batteries [24] and their state-of-health [25]. However, there has been a very limited number of studies deploying RNN models on TES systems. An interesting example related to thermal systems is available in [26], where long short-term memory (LSTM) cells are added to an RNN alongside internal gating mechanisms to predict the temperature profile of an earth-air heat exchanger. This LSTM-based RNN configuration enables handling long interval time-series data, where the gates regulate the flow of information in and out of the LSTM cell, which in turn stores information over several time-steps. The addition of LSTM cells also prevents the occurrence of vanishing gradients during the training process through backpropagation [27]. However, to the best of the authors' knowledge, LSTM-based RNN models have not been employed to estimate the SoC of an LHTES unit.

The transient variation of the SoC of a TES unit not only depends upon the mass flow rate and inlet temperature of the HTF, but also on the SoC at the previous time-step [28]. For an AI model in which SoC is an output, this implies a correlation between input and output variables. Non-linear autoregressive models with exogenous input (NARX) structures are suitable AI tools for dealing with such a correlation. While an RNN generally contains a feedback connection between hidden layers of past and present states, a NARX model instead contains a feedback connection from the output of the previous time-step that can be used along with other inputs to predict future output values.

A NARX model can be an open-loop network where the output sequence is known beforehand from experiments or other numerical models. The known output sequence is fed into the same NARX model to obtain the predicted output sequence. The other version of a NARX structure is a closed-loop network where the output sequence is not known beforehand. Here the predicted output by the NARX model in the previous time-step is used to perform the output prediction in the subsequent time-step [29]. The closed-loop network has a greater utility when the NARX model needs to be used as a standalone output predictor without any other numerical model or experimental setup incorporated to obtain the output.

Feed-forward ANNs have been mostly used for LHTES systems in the existing literature [23,30–32]. On the other hand, the capabilities of a NARX model have been demonstrated in [28] to predict the time-varying SoC of a sorption reactor. However, research focussing on the development and implementation of NARX models for LHTES units is limited. To the best of the authors' knowledge, a closed-loop NARX model that estimates SoC and the outlet temperature of the HTF of an LHTES unit is not available in the literature. To this end, this paper makes the following two major contributions:

1. A closed-loop NARX model that predicts the time-varying SoC and HTF's outlet temperature of an LHTES system is presented. This AI-based model can act as a standalone performance monitor of an LHTES unit without the need for an expensive experimental setup or a highly computationally demanding physics-based model to estimate the operational state of the thermal store. The NARX model was built on practical data from a real LHTES unit where ice is used as the storage medium. Since an ice-based LHTES unit is an economical energy storage solution widely adopted in district cooling networks [6], the NARX model presented in the paper could be highly attractive in designing future cooling networks.
2. The source code of the open-source NARX model is made freely available to contribute both to energy and AI research. Such a model is currently inexistent in popular Python libraries such as Keras (TensorFlow) [33] despite several queries in coding communities on such open-source models [34,35]. Although there have been a few implementations of NARX models using Python libraries, the available examples suffer from important issues. For instance, the

PyNeurGen's NARX model is based on Python 2, which is not supported by the latest versions of Python 3 [36]. On the other hand, the fireTS's NARX model is an open-loop network that requires the output sequence to be known beforehand [37]. Finally, GEKKO offers a linear input-output model that does not account for non-linear correlations [38]. The source code accompanying this paper relieves all these issues.

2. Material and methods

2.1. Configuration and physics-based model of the TES system under study

The selection of an ice tank is motivated by its widespread adoption in cooling systems, ranging from large district cooling systems [39] to food and pharmaceutical cold-chains [40]. This is also supported by the cost-effectiveness of the energy storage units—facilitated by the convenient crystallisation temperature of water as storage medium (i.e. the PCM) and the significant amount of latent heat which is released or absorbed during the transition between solid and liquid states.

The thermal store considered in this paper is an ICEBANK 1098C model. This is a commercial ice tank manufactured by CALMAC. It has a storage capacity of 350 kWh [41] and cooling energy is stored through ice harvesting. Within the tank enclosure, an arrangement of 68 spiralled polyethylene tubes grouped in pairs is submerged in water—forming thus 34 horizontal levels. A schematic of the internal structure of the tank is shown in Fig. 1.

The HTF is a 34% water-glycol mixture flowing through the polyethylene tubes. The release or absorption of the latent heat of water is triggered through the heat transferred between the HTF and water (or ice if in solid form). Since the HTF remains unfrozen in sub-zero temperatures, it is circulated at a temperature of −6°C to charge the tank with the aid of a compressor chiller [42]. For the discharging process, HTF circulates through the tubes at a higher temperature to extract the cooling energy stored in the tank, which is transferred by the melting of the ice.

Each pair of tubes is connected to four tube headers placed vertically as shown in Fig. 1(a). The tubes in each level are denoted as '*a*' and '*b*'. The input of the HTF for tube '*a*' is at the same end as the output of the HTF for tube '*b*' (outer headers). Similarly, the end of tube '*a*' is at the same side as the beginning of tube '*b*' (inner headers). This configuration resembles a counter-flow heat exchanger per horizontal level of the tank enabling an even solidification of water and homogeneous melting of the ice throughout. A schematic of this is shown in Fig. 2 where charging and discharging processes are illustrated.

The dimensions of the tank investigated in this paper are 2.26 m of width, 2.31 m of length, and 1.765 m of height [41]. The total volume of water in the tank is 3.71 m^3, whereas the total volume of the HTF is 0.375 m^3. This tank configuration has been adopted in a number of references available in the literature including [42], which presents an accurate one-dimensional (1-D) dynamic model of the ice tank. Nevertheless, for the experiments reported in [44,45] for the same tank a special setup was adopted, where the top 16 levels (that is, 32 tubes) were blocked to allow circulation of the HTF through the bottom 18 levels only (i.e. through 36 tubes). Thus, the volume of water was reduced to 1.9641 m^3, leading in turn to a reduction of the energy storage capacity to 174.264 kWh.

The values and dimensions of a single tube within the ice tank are summarised in Table 1. These parameters help defining the amount of water/ice wrapping the tubes in terms of cross-sectional area, external surface area, and volume.

The ice tank configuration with the parameters provided in Table 1 was modelled dynamically and verified against experimental results in [42]. The mathematical model is based on the energy conservation law, heat transfer theory, and a 1-D thermal (spatial) discretisation approach. The model was obtained considering that a pair of tubes is representative of the behaviour for all tubes in the tank. To achieve this, it is assumed that every pair of tubes has the same conditions and that viscous dissipation, radial fluid flow, axial heat conduction, external forces, and compressibility are negligible.

The energy balance equations for a single control volume of the pair of tubes considered during the modelling process are given as

$$\dot{E}_{f,a} = \rho_f V_f c_{p,f} \frac{dT_{f,a}}{dt} = \dot{m} c_{p,f} \left(T_{f,in} - T_{f,a}\right) + UA_{tr} \left(T_{w,a} - T_{f,a}\right) \tag{1}$$

$$\dot{E}_{w,a} = \rho_w V_w c_{p,w} \frac{dT_{w,a}}{dt} = UA_{tr} \left(T_{f,a} - T_{w,a}\right) + UA_{ex} \left(T_{w,b} - T_{w,a}\right) - \dot{E}_{l,a} \tag{2}$$

$$\dot{E}_{f,b} = \rho_f V_f c_{p,f} \frac{dT_{f,b}}{dt} = \dot{m} c_{p,f} \left(T_{f,in} - T_{f,b}\right) + UA_{tr} \left(T_{w,b} - T_{f,b}\right) \tag{3}$$

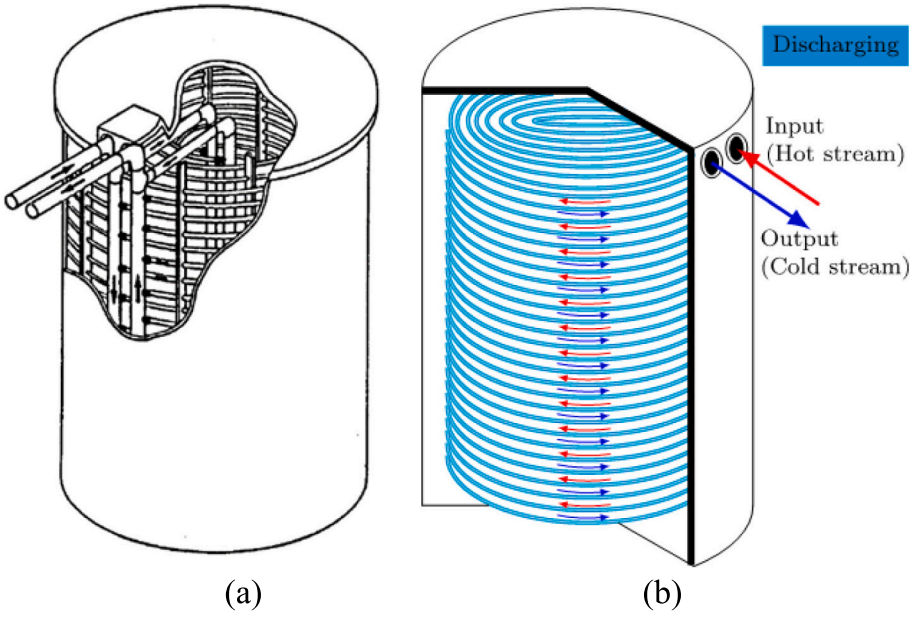

Fig. 1. (a) Internal structure of the ice tank where two external and two internal headers are shown [43]. (b) Schematic of the flow of the HTF through the internal tubes [42].

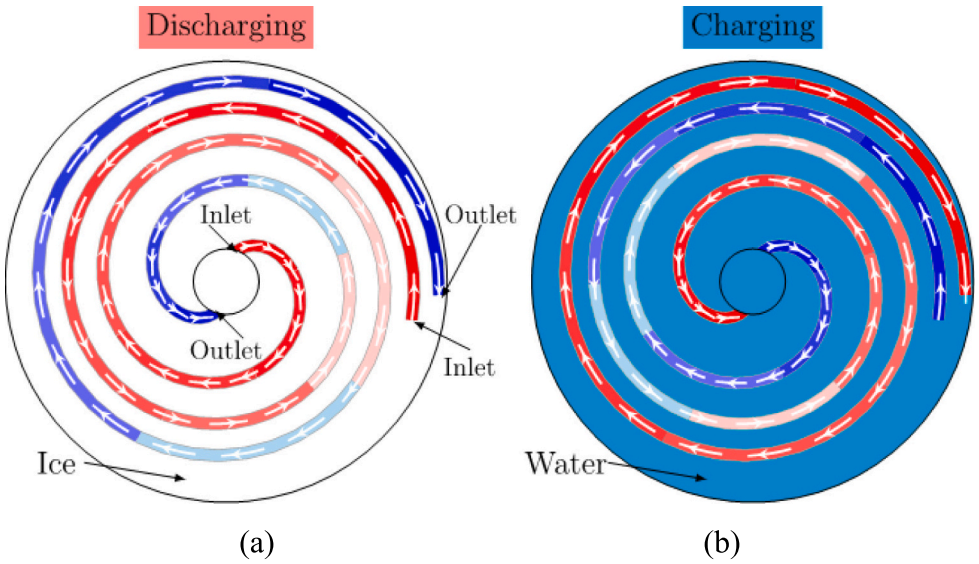

Fig. 2. Top view of a pair of tubes during (a) discharging and (b) charging processes [42].

Table 1
Parameters for a single tube of the ice tank [42].

Parameter	Symbol	Value	Unit
Tube external radius	r_o	7.9375	mm
Tube internal radius	r_i	6.35	mm
Tube hydraulic diameter	D_t	12.7	mm
Tube length	L	32.5581	m
Heat transfer area	A_{tr}	1.6238	m^2
Cross-sectional area	A_c	1.266×10^{-4}	m^2
HTF volume	V_f	0.0041	m^3
Thermal conductivity of the tube (polyethylene)	k_t	0.33	W/(m°C)
Water/ice thermal conductivity	k_w	1.35	W/(m°C)
Ice radius	r_w	23.9395	mm
Cross-sectional area of ice	A_w	0.0016	m^2
Surface area	A_{ex}	4.9	m^2
Ice volume	V_w	0.0522	m^3

$$\dot{E}_{w,b} = \rho_w V_w c_{p,w} \frac{dT_{w,b}}{dt} = UA_{tr}\left(T_{f,b} - T_{w,b}\right) + UA_{ex}\left(T_{w,a} - T_{w,b}\right) - \dot{E}_{l,b} \quad (4)$$

where $\dot{E}$ is the rate of change of energy, V is the volume, T is the temperature, U is the overall heat transfer coefficient, $\dot{m}$ is the mass flow rate, A_{tr} is the heat transfer area between the HTF and water/ice, and A_{ex} is the heat transfer area between the water/ice volumes of tubes 'a' and 'b'. Density and specific heat are defined by ρ and c_p. Subscripts 'w', 'f', 'a', and 'b' stand for water, fluid, tube 'a', and tube 'b'. $\dot{E}_l$ is an additional heat source to account for the water/ice that may not melt or solidify during discharging and charging.

The control volume used to define Eqs. (1)–(4) considers a pair of tube sections which includes the HTF volume inside each tube, the water/ice around it, and the wall of the tube through which the heat is transferred. As the model is a 1-D representation, the energy balance for the HTF circulating within the tubes describes how the mean temperature T_f of the fluid changes with respect to the x-direction alongside the tube and, additionally, how the convection heat transfer is affected by this change. Despite the simplicity afforded by the 1-D model, the overall heat transfer coefficient in the energy balance equations considers the temperature dependence of the thermophysical properties of the HTF and of water/ice—leading to a high accuracy.

A physics-based model of the ice tank using (1)–(4) was built in MATLAB/Simulink, as reported in [42], to obtain the datasets profiles for training and testing the NARX model presented in Section 2.2. As mentioned before, a thermal (spatial) discretisation method was adopted. Considering the configuration of the ice tank, tubes 'a' and 'b' are split into a defined number of nodes for discretisation and heat transfer occurs under similar conditions but with the HTF circulating in opposite directions. For a number of N nodes, the thermally discretised model would consist thus of $4N$ non-linear ordinary differential equations (i.e. the four equations given by (1)–(4) times the number of nodes). A number of 20 nodes was here adopted, leading to 80 differential equations.

Although momentum and mass balances are not considered in the physics-based model adopted in this paper, a good accuracy was obtained when the simulation results were compared with experimental data, with a maximum error of 1.64°C and a mean square error (MSE) of $0.04°C^2$ for the outlet temperature of the HTF (T_o) [42]. This performance was deemed sufficient for the purposes of this paper. Further details on the modelling considerations for the practical ice tank under study, simulation results, and experimental validation against real data available in [44,45] are provided in [42] (and references therein). To prevent duplication of published work, no further discussion on the validation of the ice tank model is here provided. Interested readers are instead referred to [42].

The physics-based model requires the discretisation of both the temporal and spatial domains to estimate the SoC of the TES unit and the outlet temperature of the HTF. The model employs an iterative solver for each node at every time-step, resulting in a considerable number of equations that must be solved across a space-time grid. This comes at the expense of a significant computational cost.

Although not specific to the ice tank adopted for this paper due to its construction and operating conditions, disregarding mass and momentum balances may not hold in scenarios incurred in other applications where high flow rates or intricate geometries induce considerable turbulence or flow reversal within the system. In such instances, the computational complexity grows significantly as solving additional transport equations pertaining to mass, momentum, and turbulence becomes imperative to map the same inputs and outputs as those of a simplified 1-D model. These limitations restrict the adaptability of physics-based models across diverse flow regimes and geometries. They underscore the value of data-driven alternatives that establish connections between inputs and outputs through general matrix multiplications rather than relying on complex differential equations to accommodate distinct thermodynamic phenomena.

2.2. Development of the AI model

2.2.1. The NARX framework

The NARX model reported in this paper consists of four ANNs in the core. This structure is schematically shown in Fig. 3. The ANNs recursively exchange their output information with each other to predict their respective future outputs. Known values of the inlet temperature of the HTF (T_i) and its mass flow rate ($\dot{m}$) are fed as exogenous inputs to the four ANNs. The actual output values of SoC (SoC) and T_o for the future time-step are assumed to be unknown while making the predictions. The model, therefore, must rely on its previous output predictions to make future predictions and is thus a closed-loop NARX model.

The general structure of the ANNs within the core of the NARX model is shown in Fig. 4(a), which shows how information propagates from the input layer to the output layer through hidden layers. Neurons in a particular layer are connected to neurons in the previous and the next layer, but not with the ones in the same layer. Fig. 4(b) shows a schematic with the general structure of a closed-loop NARX model. In this simple form, an ANN is extended with a feedback connection from the output layer, from which the information of past output values can be used along with the present input values to predict the output for the next time-step.

In general, neuron k in an ANN connects its input x_j with the output y_k through a set of weights w_{kj} and biases b_k. Mathematically, this is described by

$$y_k = \varphi\left(\sum_{j=1}^{m} x_j \times w_{kj} + b_k\right) \tag{5}$$

where φ is an activation function which introduces non-linearity between the input and the output [26].

From fundamental principles of heat transfer and thermodynamics, the SoC of a latent heat thermal store is defined in terms of the specific latent heat Δh_l, which stands for the amount of energy required per unit of mass to produce a phase transition in a PCM [48]. This energy can be determined from the relationship between specific heat of the PCM as a function of temperature, which is normally provided by PCM manufacturers as a curve, and considering the temperature boundaries of the transition zone where the phase change occurs. For clarity, these temperatures are denoted as T_{empty} and T_{full}. From [7], integrating this graphic relationship of specific heat against temperature from T_{full} (i.e. when all PCM would be crystallised as ice) to the actual temperature T_w of the PCM divided by Δh_l yields the remaining latent heat stored by the PCM. When the melting temperature T_{empty} of the PCM has been exceeded, this implies the thermal store has been fully discharged. Mathematically, for each node in the tank, and considering the notation in (1)–(4), SoC is thus expressed as

$$SoC_T(T) = \begin{cases} 0, \text{ when } T_w > T_{\text{empty}} \\ 1 - \left[\dfrac{\int_{T_{\text{full}}}^{T_w} c_{p,w}(T)dT}{\Delta h_l}\right], \text{when} T_{\text{full}} \le T_w \le T_{\text{empty}} \\ 1, \text{ when } T_w < T_{\text{full}} \end{cases} \tag{6}$$

For the ice tank model presented in Section 2.1, Δh_l is restricted by $T_{\text{full}} = -5.7°C$ and $T_{\text{empty}} = 0°C$. If (6) is used for all N PCM node temperatures, the SoC of the total PCM volume within the ice tank is

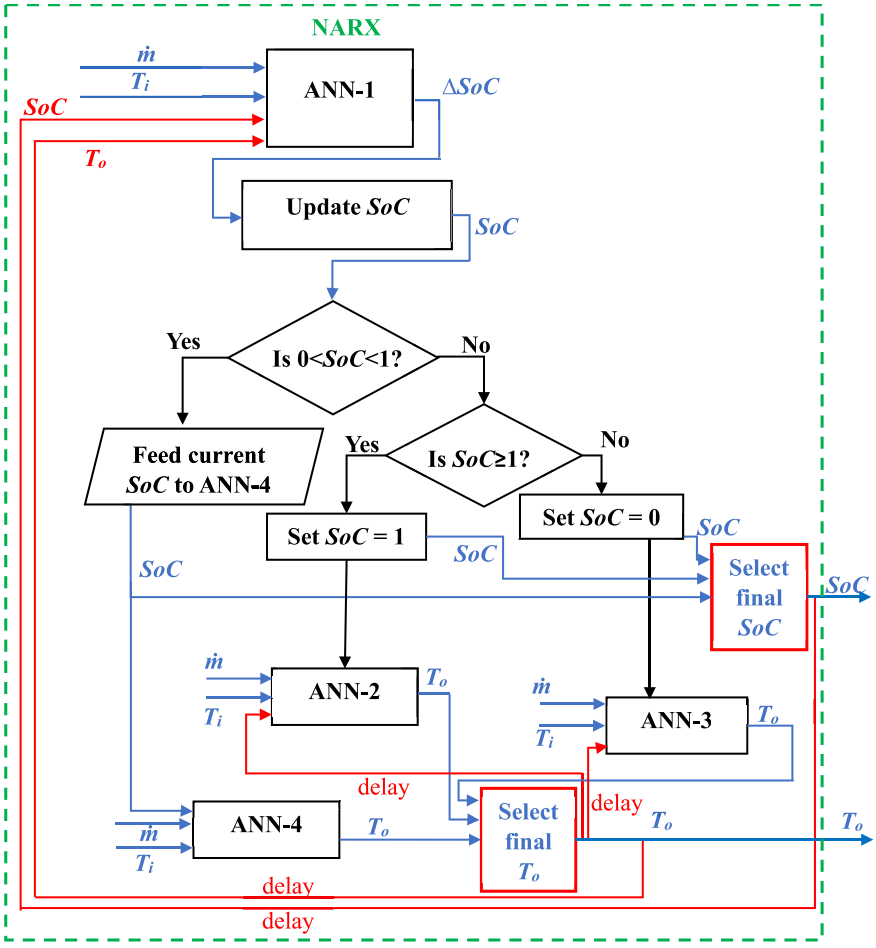

Fig. 3. Structure of the NARX model developed in this paper. The blue lines represent data flow, the black lines process flow, and the red lines data flow with delay. (For interpretation of the references to colour in this figure legend, the reader is referred to the web version of this article.)

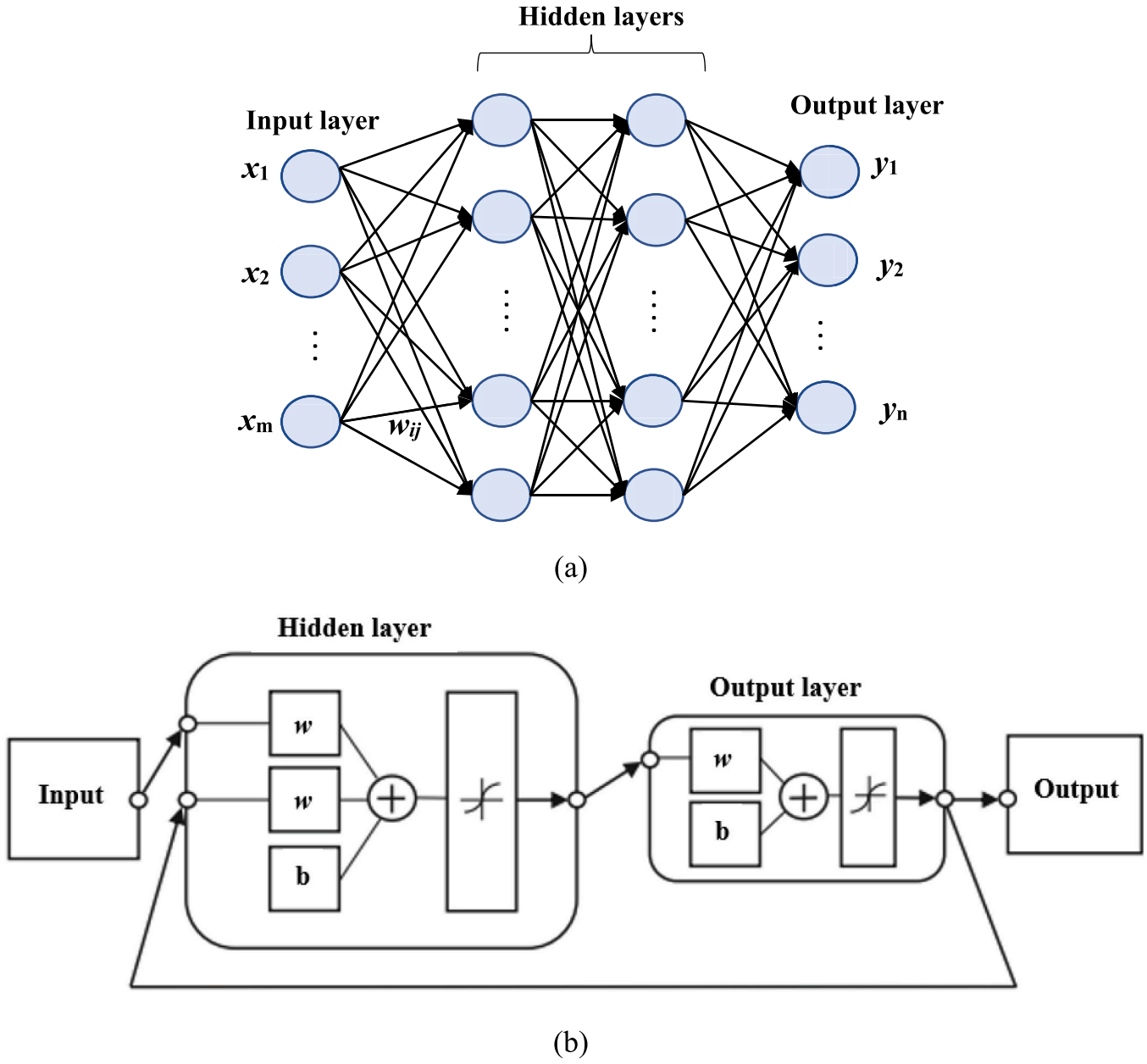

Fig. 4. (a) General architecture of an ANN [46]. (b) General architecture of a closed-loop NARX model [47].

calculated as [49].

$$SoC = \frac{\sum_{i=1}^{N} SoC_{T_{w,i}}}{N} \tag{7}$$

where $T_{w,i}$ is the temperature at node i. Interested readers are referred to [7] for further details on the SoC calculation method.

The change in SoC (ΔSoC) of the LHTES unit at each time-step is associated with the mass flow rate of the HTF, its change in temperature (which in turn depends on the HTF's inlet and outlet temperatures), and SoC at the previous time-step. This is mathematically expressed as

$$\Delta SoC(t) = f_1\{\dot{m}(t-1), T_i(t-1), T_o(t-1), SoC(t-1)\} \tag{8}$$

where function f_1 is approximated through ANN-1 as shown in Fig. 3. SoC for the subsequent time-step is then calculated with

$$SoC(t) = SoC(t-1) + \Delta SoC(t) \tag{9}$$

While updating SoC using (9), a physical constraint is imposed on the maximum and minimum possible values of $SoC(t)$. This is done through a conditional '*if*' statement. This is mathematically expressed as

$$SoC(t) = \begin{cases} 0, & \text{if } SoC(t) \leq 0 \\ 1, & \text{if } SoC(t) \geq 1 \end{cases} \tag{10}$$

In this paper, to denote a fully charged TES tank (i.e. with SoC of 100%), $SoC = 1$ is adopted, while $SoC = 0$ implies that the tank is fully discharged (i.e. with SoC of 0%). Thus, a partially charged tank will have a value of SoC between 0 and 1. In addition, the rate of change of T_o will vary depending upon whether the LHTES unit operates in latent heat mode (when $0 < SoC(t) < 1$) or sensible heat mode (when $SoC = 0$ or $SoC = 1$). In the latent heat mode, for any heat absorbed by the TES unit or released from it, the temperature of the storage medium changes at a marginal rate. This means that if $\dot{m}$ and T_i do not vary considerably in a certain time interval, T_o will not change significantly. In contrast, if the TES unit is in a sensible heat mode, even for negligibly changing values of T_i and $\dot{m}$ over time, T_o can change significantly as the heated water or cooled ice will undergo a change in temperature as a result of heat

absorption or release. This, in turn, can change the temperature gradient between the HTF and PCM.

Based on the previous discussion, the task of predicting T_o is divided according to three physical states of the TES tank: solid, liquid, and phase transition. These physical states are mathematically described by

$$T_o(t) = f_2\{T_i(t-1), T_o(t-1), \dot{m}(t-1), T_i(t), \dot{m}(t)\}, \text{when } SoC(t) = 1 \quad (11)$$

$$T_o(t) = f_3\{T_i(t-1), T_o(t-1), \dot{m}(t-1), T_i(t), \dot{m}(t)\}, \text{when } SoC(t) = 0 \quad (12)$$

$$T_o(t) = f_4\{\dot{m}(t), T_i(t), SoC(t)\}, \text{when } 0 < SoC(t) < 1 \quad (13)$$

Functions f_2, f_3, and f_4 in (11)–(13) are the non-linear functions represented through ANN-2, ANN-3, and ANN-4 within the NARX model shown in Fig. 3. In (11) and (12), the values of T_i, T_o, and $\dot{m}$ from the previous time-step are used as an indicator of how hot the sensibly heated water is (or how cold the sensibly cooled ice is) when the TES tank operates in the sensible heat mode. As the temperature of the storage medium changes marginally when the TES tank is in the latent heat mode, the values of T_i, T_o, and $\dot{m}$ from previous time-steps are not used as additional inputs. They are however replaced by the present value of SoC to capture the marginal variations in T_o with changes in SoC.

The output of ANN-1 (ΔSoC) is first updated with (9) to obtain the updated value of SoC, which in turn is fed as an input to ANN-2, ANN-3 or ANN-4 to predict T_o. After this, the output T_o from either ANN-2, ANN-3 or ANN-4 is fed as an input to ANN-1 for predicting ΔSoC for the next time-step. For its initialisation, the NARX model requires the initial values of SoC and T_o only. Due to its autoregressive properties, it will then be able to independently make future predictions indefinitely as long as $\dot{m}$ and T_i are known.

2.2.2. Dataset for training and testing the NARX model

The holistic overview of the process for developing the NARX-based SoC predictor is illustrated in Fig. 5. The initial dataset required to train the ANNs within the NARX model consists of four variables: $\dot{m}$, T_i, SoC, and T_o. To obtain suitable values of SoC and T_o for the training process, the physics-based model described in Section 2.1 was simulated using diverse profiles for $\dot{m}$ and T_i. Accordingly, 8 random profiles were generated for $\dot{m}$ and T_i. Each profile has a 24-h duration with a resolution of 1 s. Out of the 8 total profiles, profiles 1–4 were used for training ANN-1 and ANN-4, where SoC varies between 0 and 1. This enables dedicated training during the phase transition zone. Profiles 5–6 were used for training ANN-3, where $SoC = 0$ almost throughout the cycle duration. This enables training when the storage medium is in liquid state and the thermal store is completely discharged. Similarly, profiles 7–8 were used for training ANN-2, where $SoC = 1$. This facilitates training when the thermal store is completely charged and the storage medium is fully solidified. Such a profile spread allocation enables dedicated training of the ANNs constituting the NARX model.

The resulting profiles for SoC and T_o following simulation of the physics-based model with the input profiles are shown in Fig. 7. The output variables shown were then consolidated with the corresponding input variables to create the dataset for training the NARX model.

Profiles 9–19 were adopted to test the NARX model on unseen data. These profiles are shown in Figs. 8 and 9. Out of these, profiles 9–14 for $\dot{m}$ and T_i were randomly generated and then simulated with the physics-based model to obtain the profiles for SoC and T_o. These output profiles were used then as targets to benchmark the predictions of the trained

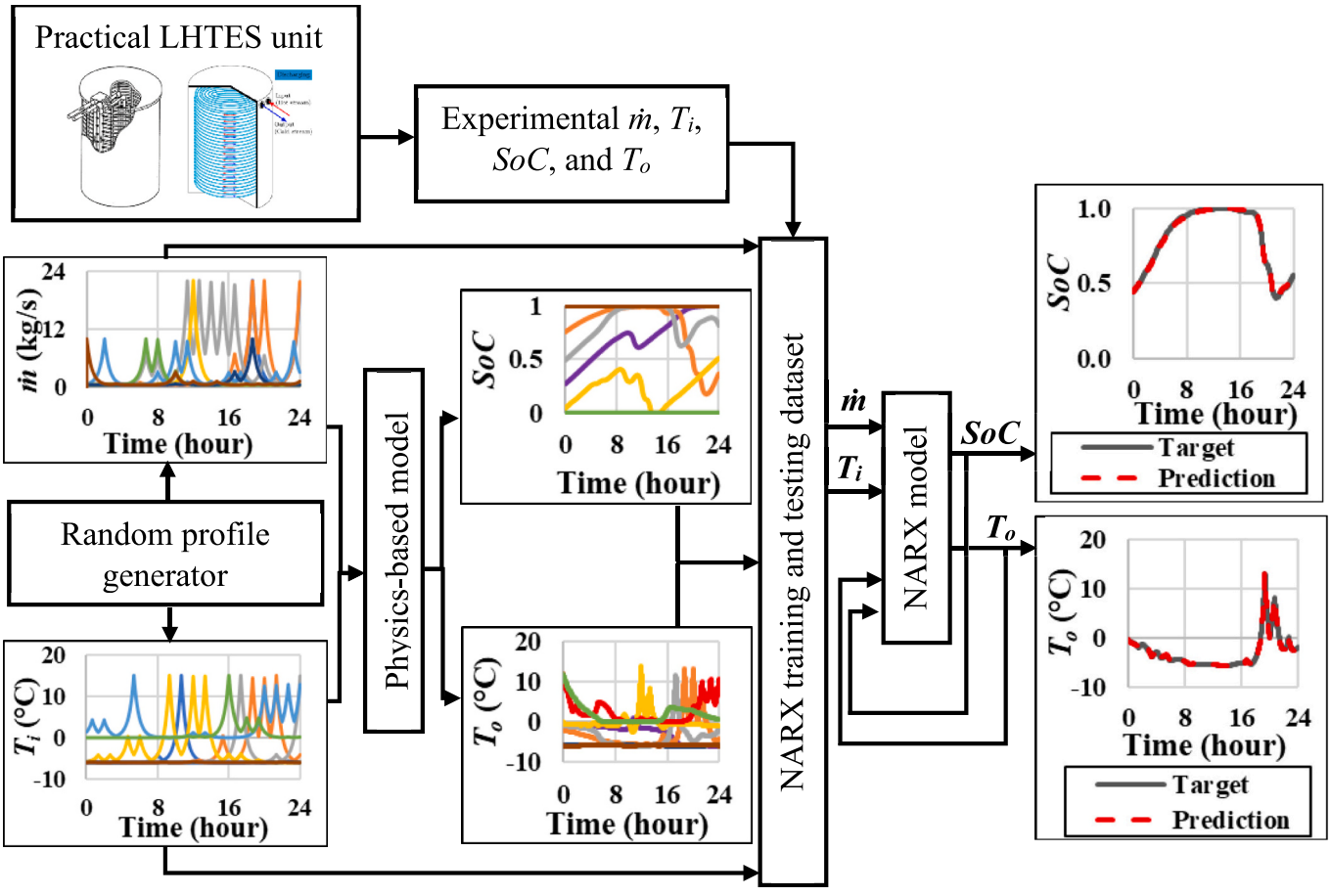

Fig. 5. Process flowchart for developing the AI-based predictor for SoC and T_o.

NARX model when profiles 9–14, not seen by the NARX model during training, were fed as inputs to make predictions.

In parallel, profiles 15–19 in Fig. 9 were obtained from experimental measurements of the practical TES unit and were only used for testing the performance of the NARX model (but not for training). This experimental dataset consists of 4 different profiles for discharging the tank (profiles 15–18) and 1 profile for charging it (profile 19). The respective experimental profiles for *SoC* and T_o were used for assessing the prediction performance of the NARX model on experimental data. It is to be noted that the durations of the experimental profiles were not the same as the simulated datasets. These variations in duration are useful as they help determining whether the trained NARX model can handle real data with different sequence lengths.

The profiles of *SoC* and T_o corresponding to the input profiles 9–19 are presented in detail in Section 3 along with the predicted values by the NARX model. The training and testing datasets are provided as supplementary material accompanying this paper to help the interested readers build their own models. Further guidance on how to use the supplementary content is provided in Appendix B.

The ANNs inside the NARX model were developed using the *MLPRegressor* class of the scikit-learn library [50]. In turn, the NARX model was developed based on these ANNs in a Python 3 programming environment, the details of which are provided in the supplementary material. For further information on the Python library dependencies adopted for the development of the NARX model and how to use it, the reader is referred to Appendix B.

2.2.3. Prediction performance indicators of the NARX model

To evaluate the prediction performance of the NARX model, the determination coefficient R^2 and the root mean squared error (RMSE) have been adopted as accuracy indicators. These are commonly employed in the existing literature to assess the performance of AI models [26]. The mathematical expressions for these performance indicators are given as

$$R^2 = 1 - \frac{\sum_{i=1}^{n} (y_i - \hat{y}_i)^2}{\sum_{i=1}^{n} (y_i - \bar{y}_i)^2} \tag{14}$$

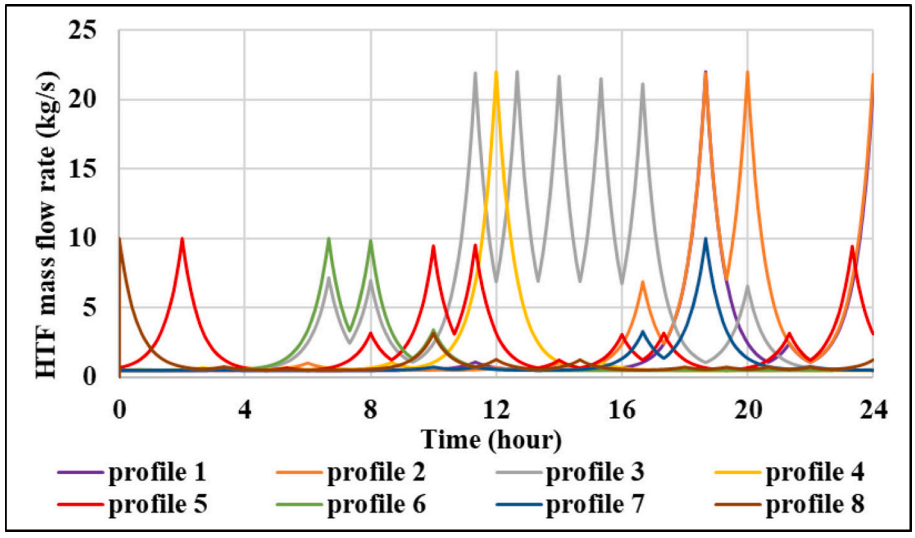

(a)

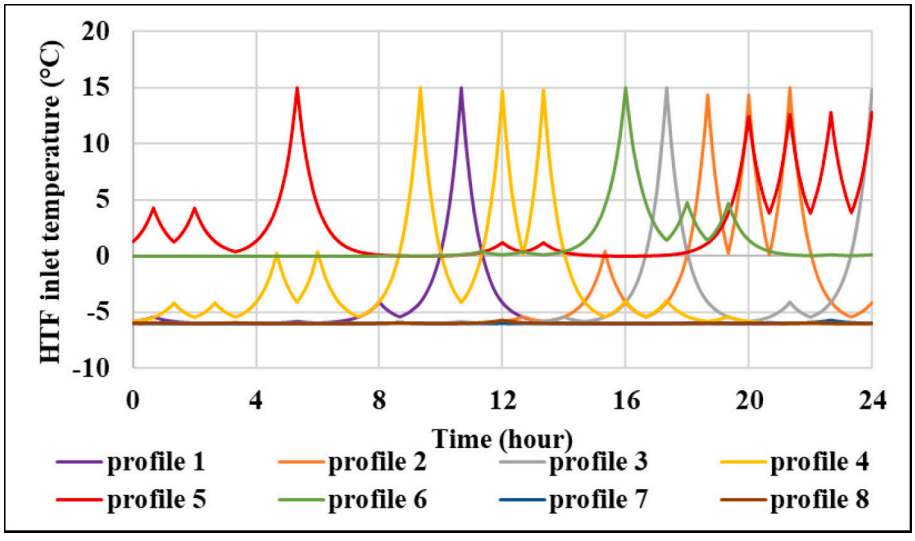

(b)

Fig. 6. Training profiles for (a) the mass flow rate of the HTF and (b) the inlet temperature of the HTF.

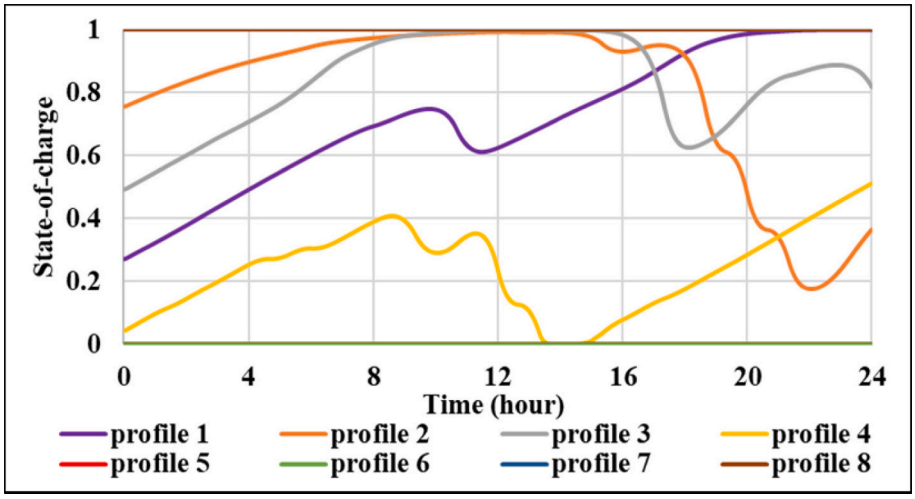

(a)

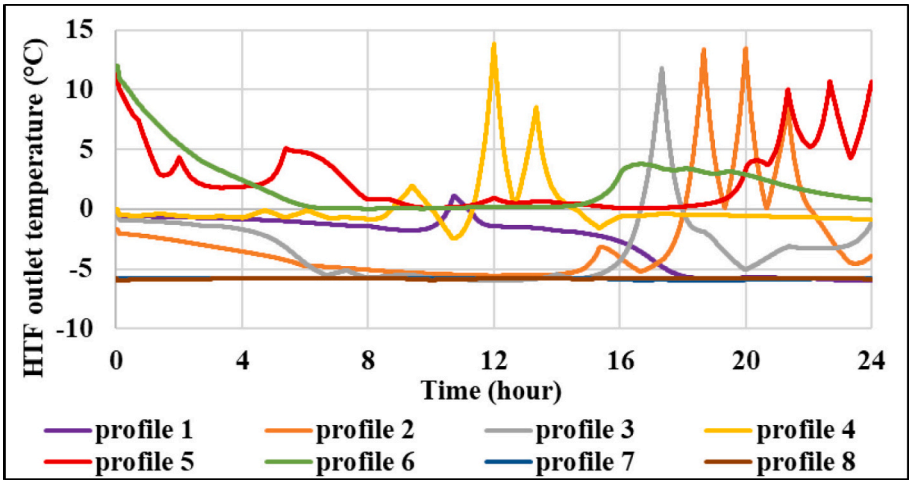

(b)

Fig. 7. Training profiles for (a) the SoC of the TES unit and (b) the outlet temperature of the HTF.

$$\text{Meansquareerror}: MSE = \frac{1}{n} \times \sum_{i=1}^{n} (y_i - \hat{y}_i)^2 \tag{15}$$

$$RMSE = \sqrt{MSE} \tag{16}$$

where y_i, $\hat{y}_i$ and $\overline{y}_i$ represent the i^{th} actual value, i^{th} predicted value, and mean of the n actual values.

2.2.4. Hyperparameter tuning of the NARX model

With the experience derived from previous work on ANN development for space cooling systems [51] and considering the high non-linearity between the input and output variables of the investigated LHTES system, a two-hidden layer architecture was initially selected for ANN-1 and ANN-4. In addition, a maximum limit of 15 neurons in each hidden layer was adopted. For the solver and activation function, three widely employed options were considered for each hyperparameter. This information is summarised in Table 2.

A large number of combinations are possible for the hyperparameters shown in Table 2. Thus, investigating each possible NARX architecture in detail would be impractical. Therefore, the Latin hypercube sampling (LHS) method along with Monte-Carlo sampling (MCS) method were employed to select random combinations of the hyperparameters. The LHS method requires a smaller number of samples than its MCS counterpart to represent a multi-dimensional parameter space. This is because of the subdivision of each parameter range into smaller intervals in the LHS method. The subsequent drawing of random samples from each of these smaller subdivisions ensures a good distribution of the samples across the entire parameter range [52]. In Table 2, the available options for neurons in each hidden layer and the random state for initialising weights and biases are considerably larger than the available options for the other hyperparameters. Therefore, the LHS method was applied to draw samples for the hidden neurons and random state. As for the other hyperparameters with fewer alternatives, the MCS method was used to draw samples.

For ANN-2 and ANN-3, which are used to predict T_o in the occasional instances of sensible cooling and sensible heating occurring in the LHTES unit, a two-hidden layer structure with 5 neurons in each hidden layer was adopted following a few heuristic trials. The 'adam' solver and the 'relu' activation function were considered. A large hyperparameter search was not conducted for these two ANNs as the NARX model was chiefly targeted for the latent heat and latent cooling modes of operation. However, these ANNs could be further tuned by the interested users by trying different hyperparameter combinations in the source code of the NARX model provided as supplementary material accompanying this paper.

The NARX model was trained with the profiles shown in Fig. 6 for

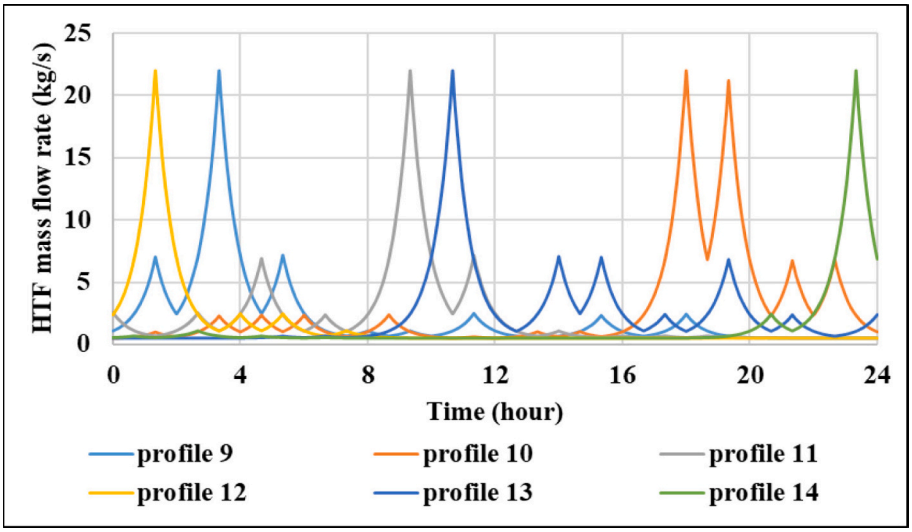

(a)

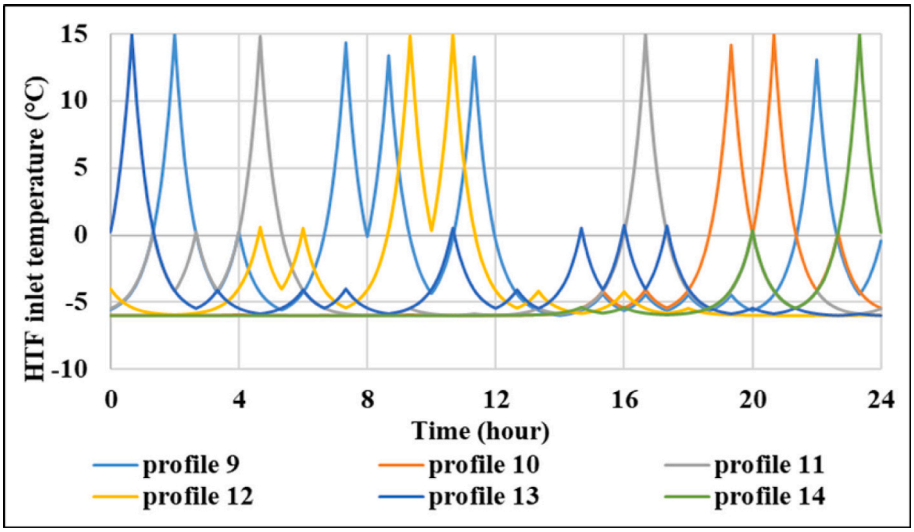

(b)

Fig. 8. Input profiles used for testing predictions: (a) mass flow rate of the HTF, (b) inlet temperature of the HTF. The respective profiles of *SoC* and T_o were obtained by simulating these input profiles with the physics-based model.

different hyperparameters of ANN-1 and ANN-4. The selection of the most suitable network architecture is discussed in Section 3.1.

2.3. Multi-criteria decision-making for selecting the best NARX configuration

As discussed in the previous section, different settings of the hyperparameters shown in Table 2 lead to a large number of possible NARX configurations. These configurations may likely exhibit a diverse performance with respect to different criteria of assessment (namely R^2 and RMSE in this paper). In such a scenario, it is possible that no particular configuration achieves the best performance in all the performance metrics when compared against other possible configurations. A suitable multi-criteria decision-making algorithm is therefore required to select the most suitable NARX architecture.

The technique for order preference by similarity to ideal solution (TOPSIS) is a widely adopted method in the literature used to select suitable models from several alternatives when no single model performs the best in all the assessment criteria [53]. The entropy-based weight assignment in TOPSIS ensures no human-introduced bias is involved in the selection of the most suitable model [54]. For a detailed explanation of this method and the significance of the steps involved in the decision-making process, interested readers are referred to [55]. For completeness, the equations of the entropy-based TOPSIS method are included next in the order of their evaluation for selecting the most suitable NARX configuration.

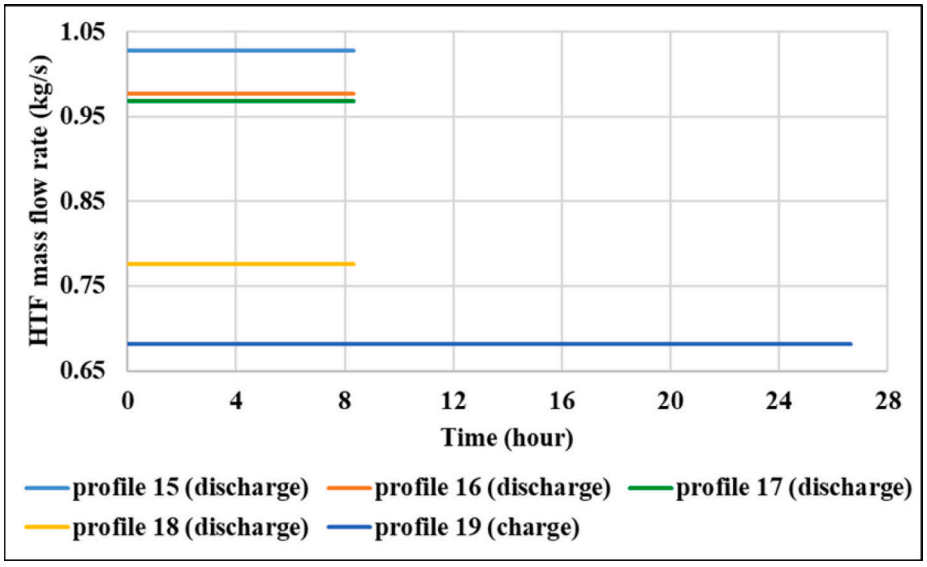

(a)

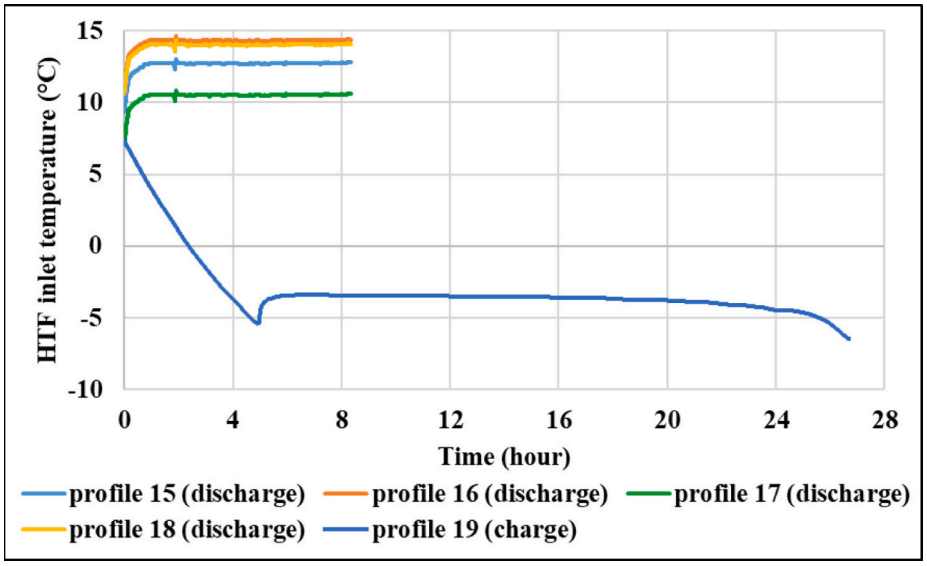

(b)

Fig. 9. Experimental profiles for (a) mass flow rate of the HTF and (b) inlet temperature of the HTF. The respective profiles of *SoC* and T_o were also obtained from experimental measurements.

$$\text{Scoring matrix : D} = \begin{bmatrix} x_{11} \ldots\ldots x_{1j} \ldots\ldots x_{1n} \\ . \quad . \quad . \\ . \quad . \quad . \\ . \quad . \quad . \\ . \quad . \quad . \\ x_{i1} \ldots\ldots x_{ij} \ldots\ldots x_{in} \\ . \quad . \quad . \\ . \quad . \quad . \\ . \quad . \quad . \\ . \quad . \quad . \\ x_{m1} \ldots\ldots x_{mj} \ldots\ldots x_{mn} \end{bmatrix} \tag{17}$$

Table 2
Hyperparameter range considered for tuning the NARX model.

Hyperparameter	Range considered
Number of hidden layers in ANN-1 and ANN-4	2
Neurons in each hidden layer of ANN-1 and ANN-4	3 to 15
Random state for initialising weights and biases of ANNs	1 to 250
Activation function	logistic, tanh, relu [50]
Solver	adam, lbfgs, sgd [50]

where D is the matrix that contains scores (x_{ij}) of m different design alternatives under n different performance assessment criteria.

$$\text{Standardised matrix : } r_{ij} = \frac{x_{ij}}{\sqrt{\sum_{i=1}^{m} x_{ij}^2}}; i = 1, 2, \ldots., m; j = 1, 2, \ldots., n \tag{18}$$

where r_{ij} is the standardised score for the element x_{ij} in D.

$$\text{Proportion matrix : } p_{ij} = \frac{x_{ij}}{\sum_{i=1}^{m} x_{ij}}; i = 1, 2, \ldots., m; j = 1, 2, \ldots., n \tag{19}$$

where p_{ij} is the proportion for the score x_{ij} in D.

$$\text{Entropy computation for } j^{th} \text{ criterion : } e_j = -\frac{1}{ln\, m}\sum_{i=1}^{m} p_{ij} \times ln\, p_{ij} \tag{20}$$

where e_j denotes the entropy for the criterion j.

$$\text{Entropy weight computation for } j^{th} \text{ criterion : } w_j = \frac{(1 - e_j)}{\sum_{j=1}^{n}(1 - e_j)} \tag{21}$$

where w_j is the weight for j^{th} criterion determined by entropy method.

$$\text{Weighted matrix computation : } v_{ij} = w_j r_{ij}; i = 1, 2, \ldots., m; j = 1, 2, \ldots., n \tag{22}$$

where v_{ij} represents the weighted score.

$$\text{Ideal solution : } A^+ = \left\{ \left(max_i x_{ij} | j \in J_1\right), \left(min_i v_{ij} | j \in J_2\right) | i = 1, 2, \ldots, m \right\} = v_1^+, v_2^+, \ldots v_n^+ \tag{23}$$

where A^+ is the ideal solution that consists of the best values for each criterion ($v_1^+, v_2^+, \ldots v_n^+$).

$$\text{Anti} - \text{ideal solution : } A^- = \left\{ \left(min_i x_{ij} | j \in J_1\right), \left(max_i v_{ij} | j \in J_2\right) | i = 1, 2, \ldots, m \right\} = v_1^-, v_2^-, \ldots v_n^- \tag{24}$$

where A^- is the anti-ideal solution that consists of the worst values for each criterion (v_1^-, v_2^-,..., v_n^-).

In (23) and (24), J_1 represents the most suitable value of criterion j when it is profitable in nature and J_2 when it is unprofitable in nature.

$$\text{Euclidian distance from ideal solution } \left(S_i^+\right) : S_i^+ = \sqrt{\sum_{j=1}^{n}\left(v_{ij} - v_j^+\right)^2}; i = 1, 2, .., m \tag{25}$$

$$\text{Euclidian distance from anti} - \text{ideal solution } \left(S_i^-\right) : S_i^- = \sqrt{\sum_{j=1}^{n}\left(v_{ij} - v_j^-\right)^2}; i = 1, 2, .., m \tag{26}$$

$$\text{Closeness degree evaluation } \left(C_i^+\right) : C_i^+ = \frac{S_i^-}{S_i^+ + S_i^-}; i = 1, 2, \ldots., m \tag{27}$$

A larger value of C_i^+ indicates a better suitability of the respective design (and vice versa). Therefore, the best design is chosen as the one that results in the largest value of C_i^+.

3. Results and discussion

3.1. Selecting a high-accuracy NARX configuration

From the options considered in Table 2, 300 random combinations of the hyperparameters were initially taken and the performance of the NARX model was recorded for each such configuration. These 300 configurations were then filtered by the prediction performance conditions $R^2_{SoC} \geq 0.95$ and $R^2_{T_o} \geq 0.95$ for each of the testing profiles obtained from the physics-based model and experiments. The configurations predominantly with 'tanh' as the activation function for ANN-4 and 'adam' as the solver for both ANN-1 and ANN-4 exhibited high values of R^2. Hence, these parameters were fixed in the next step and the remaining hyperparameters were randomly sampled again to perform a more detailed hyperparameter search. This way, 300 additional configurations were created and assessed with the testing profiles sourced from the physics-based model and experiments. Following this, the performance filter $R^2_{SoC} \geq 0.95$ and $R^2_{T_o} \geq 0.95$ was applied again to the new 300 configurations. The 23 candidate configurations that passed through this filter are presented in Table A1 of Appendix A.

To determine the relative suitability of the 23 selected candidates and to select the best configuration, the average values of R^2 and RMSE for SoC and T_o on the testing profiles were considered as the judging criteria. The entropy-based TOPSIS method described in Section 2.3 was used to rank the candidates according to these criteria, with results shown in Table A2 of Appendix A. In the table, the relative rankings of the 23 filtered configurations are included. The configuration for Case 82 is the most suitable—exhibiting average values of $R^2_{SoC} = 0.9943$ and $R^2_{T_o} = 0.9842$ and average values of RMSE of 1.73% for SoC and 0.3161°C for T_o over all the testing profiles sourced from the physics-based model and experiments. The average prediction time for all the testing profiles by all the configurations assessed during hyperparameter tuning ranged between 12 s to 16 s. The prediction time slightly changed within this given range for the same configuration under different runs depending upon the overall CPU usage in the computer where the NARX model was executed.

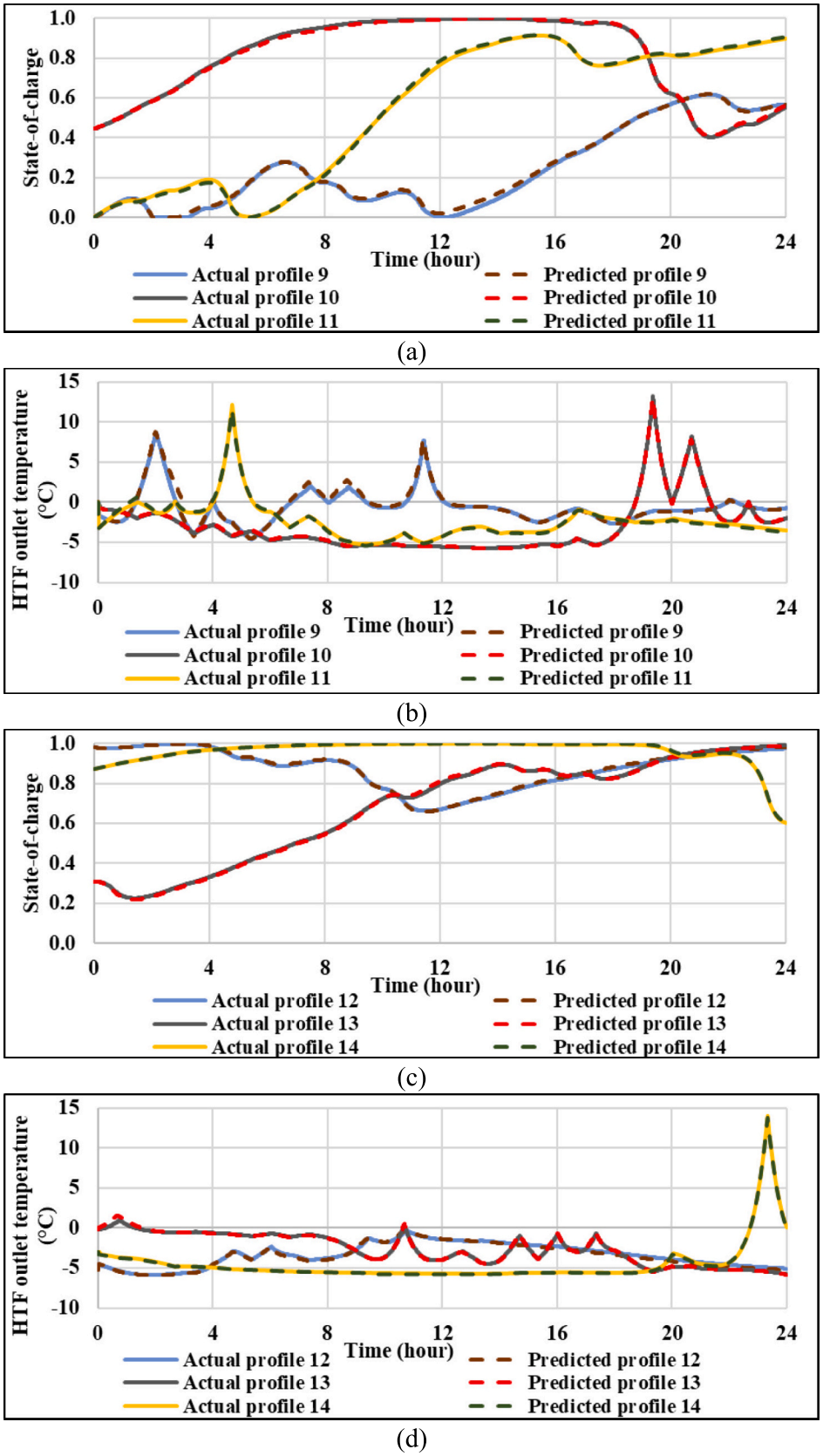

Fig. 10. Predictions of the NARX model on unseen test profiles sourced from the physics-based model. Profiles 9 to 11: (a) SoC, (b) outlet temperature of the HTF. Profiles 12 to 14: (c) SoC, (d) outlet temperature of the HTF.

3.2. Predictions on unseen profile data

The predictions made on the testing profiles by the best NARX configuration (Case 82 in Table A2 in Appendix A) are presented in this section. Fig. 10 presents a comparison between the output profiles predicted by the NARX model (provided with dashed traces) and those obtained with the physics-based model (solid traces) for the same input profiles. To demonstrate the performance of the NARX model to

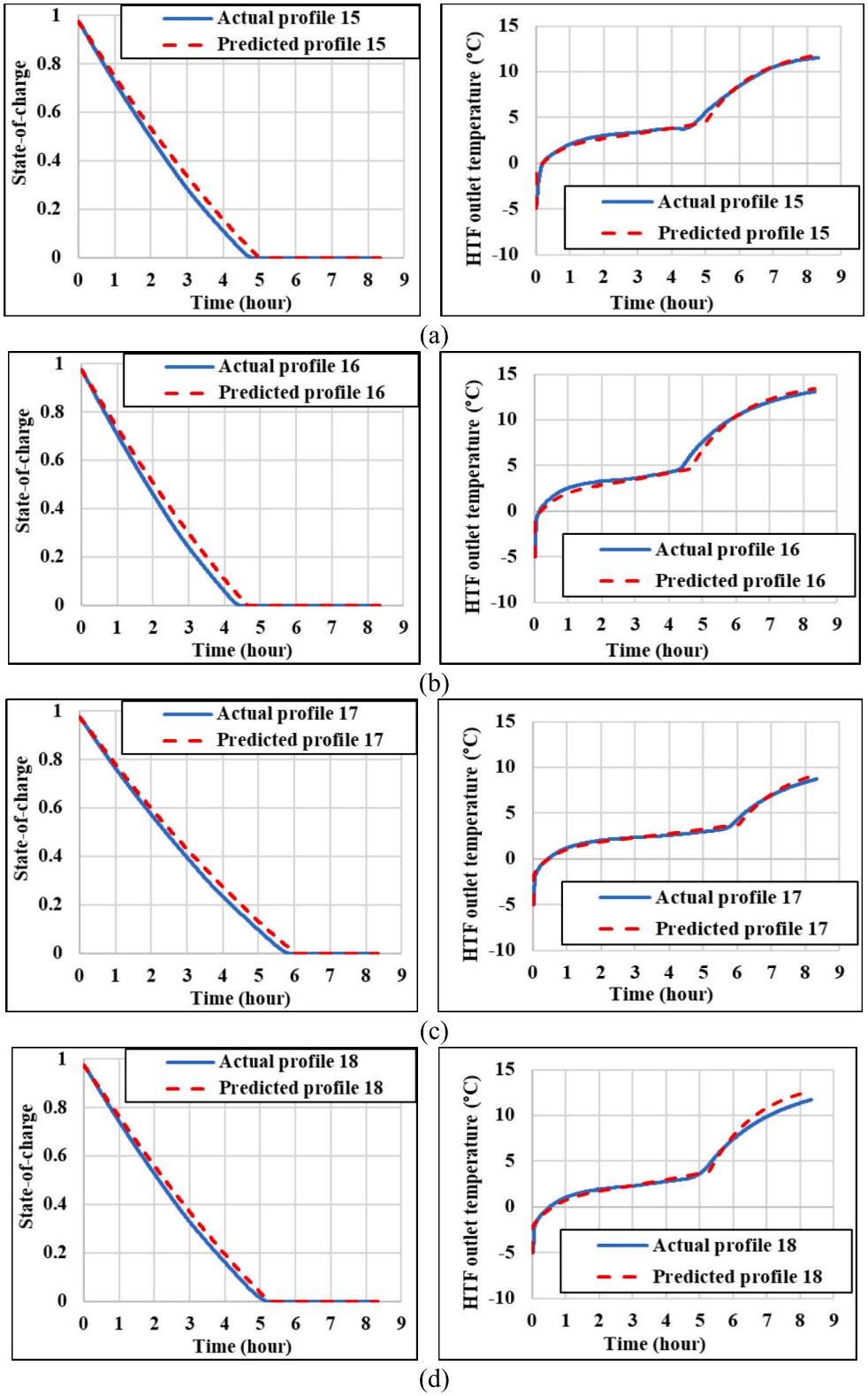

Fig. 11. Predictions of the NARX model on unseen test profiles sourced from discharging experiments of the practical TES unit: (a) Experiment 1 (with profile 15); (b) Experiment 2 (with profile 16); (c) Experiment 3 (with profile 17); (d) Experiment 4 (with profile 18). *SoC* predictions are shown to the left and T_o predictions to the right.

accurately predict output profiles irrespective of variations in the initial conditions, four out of the six text profiles consider initial values of SoC amenable to a partially charged thermal store—see profile 10 in Fig. 10 (a) with an initial $SoC = 0.45$, and profiles 12, 13 and 14 in Fig. 10(c) with initial values for SoC of 0.98, 0.31 and 0.87.

From simple observation of the results shown in Fig. 10, it is evident that the NARX model achieves a prediction of SoC and T_o in very close proximity to the physics-based model. This is quantitatively supported by the high values of R^2 (0.9979 for SoC and 0.9898 for T_o) and low values of RMSE (0.72% for SoC and 0.1771°C for T_o) achieved by the NARX model when compared with the testing profiles obtained from the physics-based model. Furthermore, the time required for the NARX model to predict the output profiles for the operation of an entire diurnal cycle of the TES tank was about 16 s. To estimate the same output profiles, the physics-based model took instead about 119 s, which represents an increase by 86% compared to the NARX model. Such a reduction in the estimation time of the operational state of the TES tank achieved by the NARX model could be highly useful to perform transient simulations for large energy networks involving several systems for storage, production, and consumption of energy.

To further evaluate the performance of the NARX model, its prediction values were compared against the results of practical experiments obtained from [44,45]. To this end, the recorded measurements of T_o and SoC from the real ice tank (as presented in Section 2.1) were used for benchmarking the predictions of the NARX model for the same output parameters. The experimentally measured $\dot{m}$ and T_i in each discharging process were fed as an input to the NARX model.

Fig. 11 shows the comparison of the 4 different discharging experiments. The output profiles predicted by the NARX model are in good agreement with the experimental results for the discharging processes. The prediction time was about 6 s as these profiles are shorter than a complete diurnal cycle.

For charging of the TES tank, only one set of experimental results was available in [44,45]. Fig. 12 compares the prediction of the NARX model against experimental results for the charging process. As with the comparison conducted for discharging processes, the experimentally measured values of $\dot{m}$ and T_i were used as inputs. The NARX model captures the variations in the output profiles with a high accuracy. In this case, the prediction time for the charging profile was about 18 s as the charging cycle is longer than a diurnal cycle.

A quantitative analysis was conducted to further assess the prediction performance of the NARX model to complement the results shown in Figs. 11 and 12. The NARX model achieves average values of $R^2_{SoC} = 0.99$ and $R^2_{T_o} = 0.9774$ and RMSE values of 2.95% and 0.4829°C for SoC and T_o when compared with the experimental datasets for charging and discharging. The maximum RMSEs were observed with the experimental charging profile 19, with values of 3.65% for SoC and 0.5818°C for T_o. Conversely, the minimum RMSEs were 2.36% for SoC (in the experimental discharging profile 18) and 0.3338°C for T_o (in the experimental discharging profile 17). The NARX model thus maintains a consistent accuracy in prediction with an arguably marginal gap between the maximum and minimum errors.

3.3. Comparison of NARX model with a non-linear observer

To provide further confidence on the capabilities of the NARX model to predict the dynamic behaviour of an ice tank, a comparison was conducted against the performance afforded by the non-linear observer reported in [7]. This comparison enables assessing the potential of employing the NARX model for the continuous monitoring of the dynamic operation of a thermal store with respect to an estimation methodology based on modern control theory available in the literature. A brief overview of the non-linear observer and its structure is provided next.

A state observer, or state estimator, is a computer-implemented dynamic system employed to estimate the internal state of the system under study from measurements of its inputs and outputs [56]. For an LHTES unit, a state observer may be used to provide an estimation of the temperature gradient of a PCM by employing the input and output temperature and mass flow rate of the HTF which circulates within the unit. For the ice tank, given the high non-linearities arising from the temperature dependence of the thermophysical properties of the PCM and the HTF, a non-linear structure must be adopted.

The physics-based model of the ice tank is described in state-space form as

$$\begin{aligned} \frac{\mathrm{d}}{\mathrm{d}t}\mathbf{x} &= f(\mathbf{x},\mathbf{u}), \\ \mathbf{y} &= j(\mathbf{x}) \end{aligned} \tag{28}$$

where $\mathbf{u}$, $\mathbf{x}$, and $\mathbf{y}$ denote the input, state, and output vectors and the top equation represents the set of non-linear ODEs of the dynamic model described by (1)–(4) in Section 2.1. In the bottom equation, $j(\mathbf{x})$ is a scalar output, which is the HTF output temperature. For an ice tank spatially discretised into 20 nodes, the model is described by a set of 80 non-linear ODEs, with a state vector given as

$$\mathbf{x} = \left[T_{f,1,a}\ \ T_{w,1,a}\ T_{f,1,b}\ \ T_{w,1,b}\cdots T_{f,20,a}\ \ T_{w,20,a}\ T_{f,20,b}\ \ T_{w,20,b}\right] \tag{29}$$

The input vector is defined as

$$\mathbf{u} = \left[\dot{m}\ \ T_{f,in}\right] \tag{30}$$

where $T_{f,in}$ is the input temperature of the HTF and $\dot{m}$ is the total mass

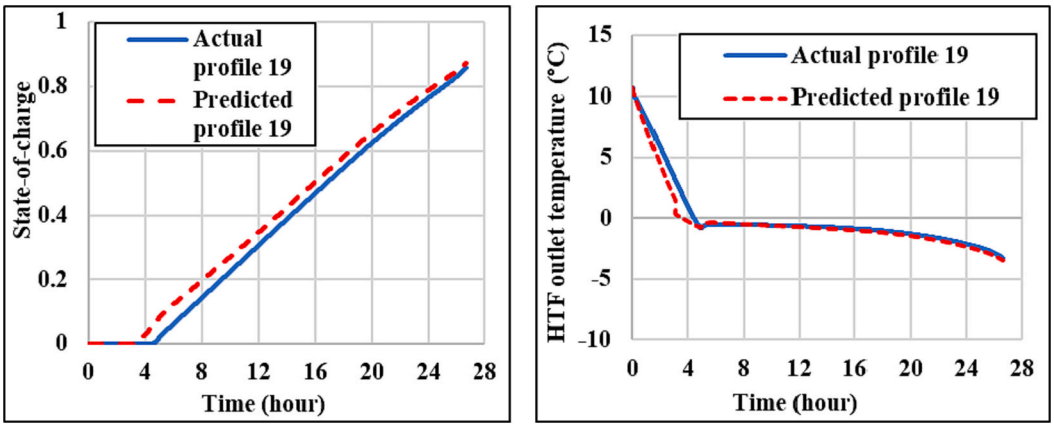

Fig. 12. Predictions of the NARX model on unseen test profiles sourced from a charging experiment (profile 19). SoC predictions are shown to the left and T_o predictions to the right.

flow rate entering the ice tank divided by the total number of tubes. Because of the internal configuration of the tank, shown in Fig. 1, there are two system outputs, which in a practical tank would merge through system headers to form a unique output [42]. These are the temperatures of the HTF at the opposite ends of the tubes and the observer must consider both. Since the inlet of tube '*a*' and the output of tube '*b*' are located in the first node, and given the outlet of tube '*a*' and the inlet of tube '*b*' are located in the final node 20, the output vector is defined as

$$\mathbf{y} = \left[T_{f,1,b}\ T_{f,20,a}\right] \tag{31}$$

The observer structure for (28) is defined as [56]

$$\frac{\mathrm{d}}{\mathrm{d}t}\hat{\mathbf{x}} = f(\hat{\mathbf{x}}, \mathbf{u}) + \mathbf{J}(\mathbf{y} - j(\hat{\mathbf{x}}))\ \tag{32}$$

In (32), $\hat{\mathbf{x}}$ represents the estimated state vector, while $\mathbf{J}$ denotes a diagonal matrix with constant coefficients. In general, the design of $\mathbf{J}$ must be conducted so that the estimation error for all states converges to zero, that is, $\mathbf{e} = \mathbf{x} - \hat{\mathbf{x}} = \mathbf{0}$. The observer is also defined using the same differential equations of the system model given by (28). As discussed in [7], the diagonal entries of $\mathbf{J}$ were obtained heuristically and set to a value of 0.5.

A schematic of the non-linear observer for the ice tank is provided in Fig. 13. For further information on the observer derivation, implementation, and design, the interested readers are referred to [7]. The same reference provides a comprehensive verification of the non-linear observer performance against data available in the literature. To prevent duplication of published work, no further discussion on the observer validation is further provided in this paper.

To conduct the comparative exercise between the NARX model and the non-linear state observer, the test profiles 9 and 10 were adopted. The values of T_i and $\dot{m}$ for these profiles (shown in Fig. 8) were used as inputs for the NARX model as well as for the non-linear state observer. The results for the non-linear observer were obtained with an AMD Ryzen 7 7730 U CPU @ 2.0Ghz with 16 GB of RAM, whereas those for the NARX model were obtained with an Intel i7 11700 CPU @ 2.50Ghz with 16 GB of RAM.

The estimated output profiles of *SoC* and T_o predicted by both the NARX model and the non-linear state observer are shown in Fig. 14. The non-linear observer exhibited smaller prediction errors, with an RMSE of 0.08% in *SoC* prediction of profile 9 and 0.16% for the profile 10. For T_o, these errors were 3.21×10^{-6}°C and 0.0015°C. In contrast, the NARX model exhibited RMSEs of 1.18% and 0.66% for *SoC* while for T_o these errors were 0.3685°C and 0.1165°C. While both models demonstrated reasonably small prediction errors, the non-linear state observer outperformed the NARX model in terms of accuracy. This result was expected, as a well-designed observer guarantees an estimation error (in this case of temperatures) asymptotically converging to zero.

However, the NARX model demonstrated advantages in computational efficiency. While the non-linear state observer took ~54 s to predict profile 9 and ~35 s to predict profile 10, the NARX model took ~16 s to predict each profile. These results demonstrate that the NARX model is capable of reducing the computation time by up to 70.4% (for profile 9) compared to the solution based on modern control theory. Despite a marginal compromise in accuracy, the NARX model offers significant computational speed gains in predictions.

3.4. On the integration of physics-informed attributes into the NARX model

The NARX model investigated so far divides the prediction task among different ANNs based on whether the TES tank is in a phase transition, sensible cooling, or sensible heat state of operation. To understand how these physics-informed attributes help in improving the overall prediction accuracy, a comparison was carried out between two versions of the NARX model with varying complexity. The first version of the model is the one already shown in Fig. 3, which has 4 ANNs in the core.

Fig. 15 shows the second version of the NARX model. Compared to the first model, ANN-2 and ANN-3 previously used for predicting T_o in the sensible cooling and sensible heat conditions have been removed. To make this alternative model operational, the sensible cooling and sensible heat training profiles shown in Fig. 6 (profiles 5–8) were merged with the latent heat/latent cooling training profiles (profiles 1–4). ANN-4 was subsequently trained on the merged dataset to make predictions of T_o over all the latent and sensible heat-cooling conditions of the TES unit.

To compensate for the loss of trainable parameters in the alternative NARX model shown in Fig. 15, the size of ANN-4 was increased to allow three times the maximum number of neurons per hidden layer (i.e. with a maximum of 45 neurons per hidden layer). Another hyperparameter search was conducted for ANN-1 and ANN-4 as explained in Section 3.1 by setting the solver to 'adam' for both the ANNs and the activation function to 'tanh' for ANN-4. In this case, 300 such candidate configurations were tested accordingly including a scenario where the hyperparameter settings were kept exactly the same for ANN-1 and ANN-4 as in the previous best configuration (Case 82 in Table A2).

Although several of the candidate configurations achieved an average $R^2_{SoC} \geq 0.95$ over the testing profiles, none was able to achieve $R^2_{T_o} \geq 0.95$. Table A3 in Appendix A lists the accuracy metrics of the configurations that could attain average $R^2_{SoC} \geq 0.95$ and a reduced $R^2_{T_o} \geq 0.7$ along with the case with hyperparameters similar to Case 82 in Table A2. TOPSIS was used to rank these selected configurations, with Case 152 being selected as the most suitable. This was adopted for a more detailed comparison with the first version of the NARX model. In addition, another configuration (Case 176), ranked 2nd by TOPSIS, was also used for examining the predictions of the alternative version of the NARX model. This is because ANN-4 in this case contains a significantly

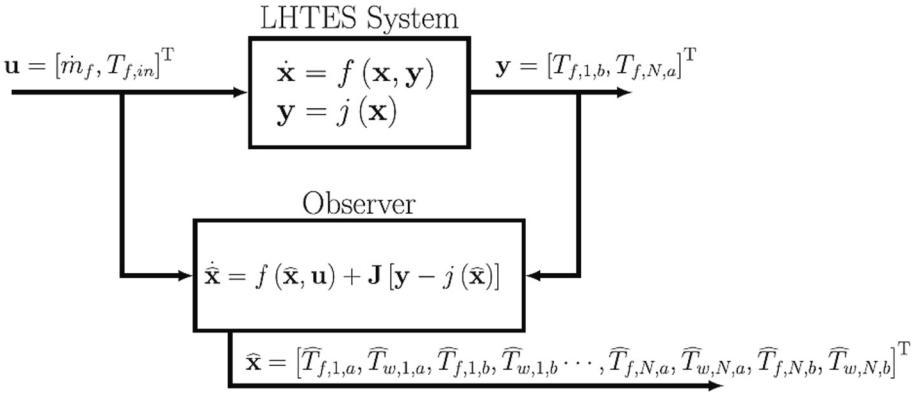

Fig. 13. Non-linear state observer for an ice tank [7].

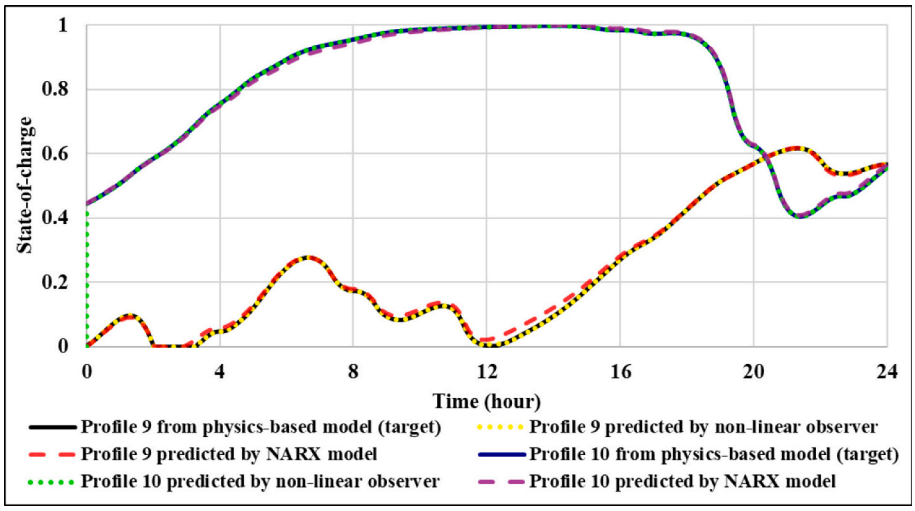

(a)

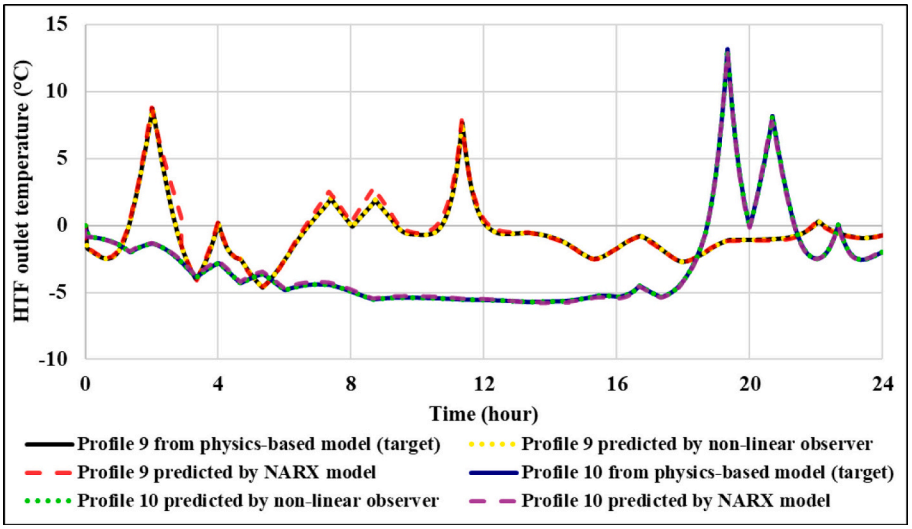

(b)

Fig. 14. Comparison of the prediction of (a) *SoC* and (b) T_o by the NARX model and the non-linear state observer reported in [7].

larger number of hidden neurons due to the relaxation in the maximum hidden layer size.

Fig. 16 shows the predicted profiles of *SoC* and T_o for Case 152 in Table A3 of the alternative version of the NARX model for one experimental discharging cycle and for one charging cycle. For discharging, the input profile 18 in Fig. 9 was used, while for charging the input profile 19 was employed instead. Fig. 17 shows a similar comparison exercise for Case 176. Although the NARX model with 2 ANNs correctly estimates the SoC of the TES tank, it is only capable of correctly predicting T_o in the phase transition zone. In both Figs. 16 and 17, the phase transition occurs in the time interval of the 0th hour to approximately the 5th hour for the discharging profile 18, which is indicated by a continuous reduction in the value of SoC during this interval. The predictions of T_o by the second NARX model fairly match the experimental values. However, beyond the 5th hour, as the TES tank enters the sensible heat mode (indicated by $SoC = 0$), the predictions of T_o deviate significantly from the experimental values. A similar behaviour can be noticed for the charging profile 19, where sensible cooling occurs in the interval of the 0th hour to approximately the 5th hour, after which solidification of the water starts—with a corresponding continuous increase in the values of *SoC*. The predicted values of T_o deviate significantly from the experimental values in this sensible cooling period.

The first version of the NARX model, with results shown in Figs. 11 and 12, achieves a better performance in comparison to the alternative version of the model presented in this section. The physics-based division of the prediction task for different heating and cooling regimes afforded by the first model enables to outperform the alternative model where an enlarged ANN-4 accounts for both sensible and latent heat-cooling phenomena. The addition of two ANNs with only 5 neurons in each of the 2 hidden layers allows the first version of the model to achieve a higher accuracy with fewer overall trainable parameters because of the significant size reduction of ANN-4 compared to the other version of the model.

The results presented in this section illustrate how more accurate AI models could be built with less computational resource requirement than end-to-end fully surrogate models by embedding simple physics-informed principles.

3.5. On the limitations and scope of the NARX model

The NARX model presented in this paper was developed from physics-based and experimental data pertaining to the operation of a practical water-ice TES tank of 350 kWh capacity. In this system, the rate of phase transition is dependent on the mass of ice and water present in

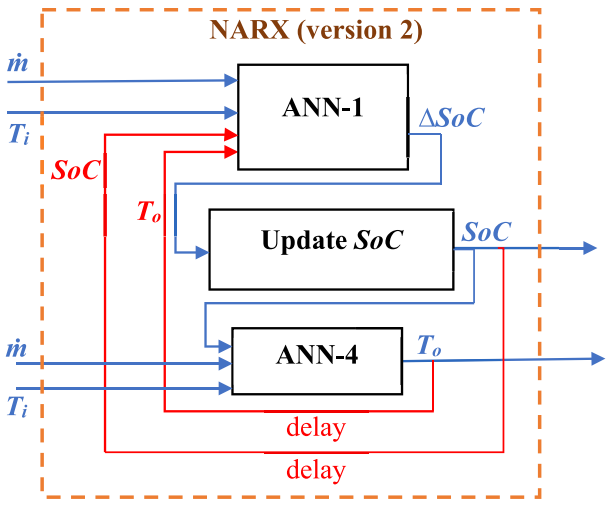

Fig. 15. Alternative NARX model with 2 ANNs. Blue lines represent general data flow and red lines represent data flow with delay. (For interpretation of the references to colour in this figure legend, the reader is referred to the web version of this article.)

the tank to absorb heat from the incoming HTF or release heat into it. The same values of $\dot{m}$ and T_i would melt or solidify a smaller fraction of ice if the overall tank size and the PCM mass contained within are increased (and vice versa). Therefore, the prediction of the AI model will be different from the actual outputs if a TES unit of a different size were to be used.

As the NARX model was trained on simulation data from a physics-based model of the ice tank, it will inherit inaccuracies present in the model of the thermal store. For example, when compared with the experimental results, the physics-based model achieved an RMSE of 0.2°C whereas this value increased to 0.483°C for the NARX model. Although both RMSE values are small in magnitude, thus indicating good accuracy for both models, the increased RMSE of the NARX model illustrates an error propagation from the source of the training data to the trained model. It is therefore important to ensure the accuracy of a physics-based model through robust experimental validation to ascertain the effectiveness of a prospective NARX-based estimator.

The NARX model is also constrained to the specific type of PCM used in the LHTES application, which for this paper is water. Other types of PCM may exhibit a hysteresis phenomenon. Under hysteresis, there may be different rates of change for temperature rise or fall for the same amount of heat exchange depending upon whether heat is being added or extracted from the PCM. This may lead to different specific heat-temperature curves for charging and discharging processes, which would affect the performance of the current NARX model. Thus, additional information on the temporal derivative of temperature may be

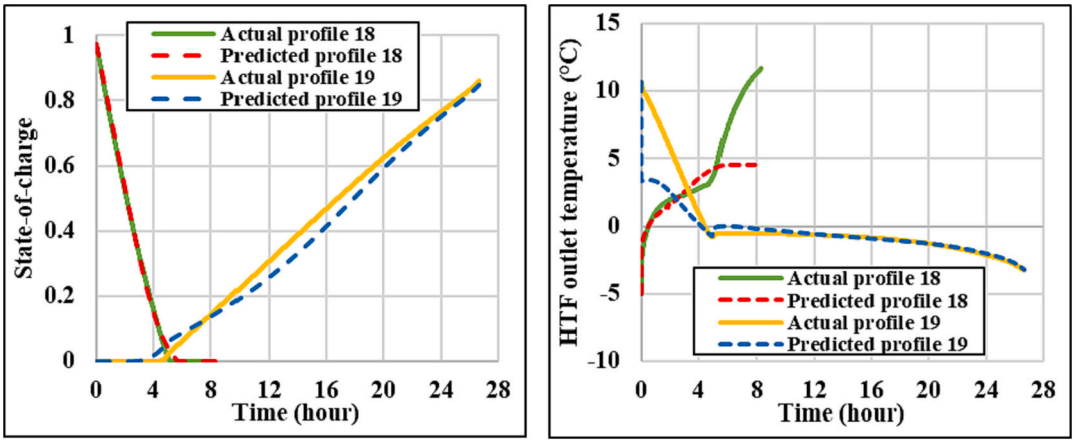

Fig. 16. *SoC* and T_o predictions by the NARX model with 2 ANNs (Case 152 in Table A3).

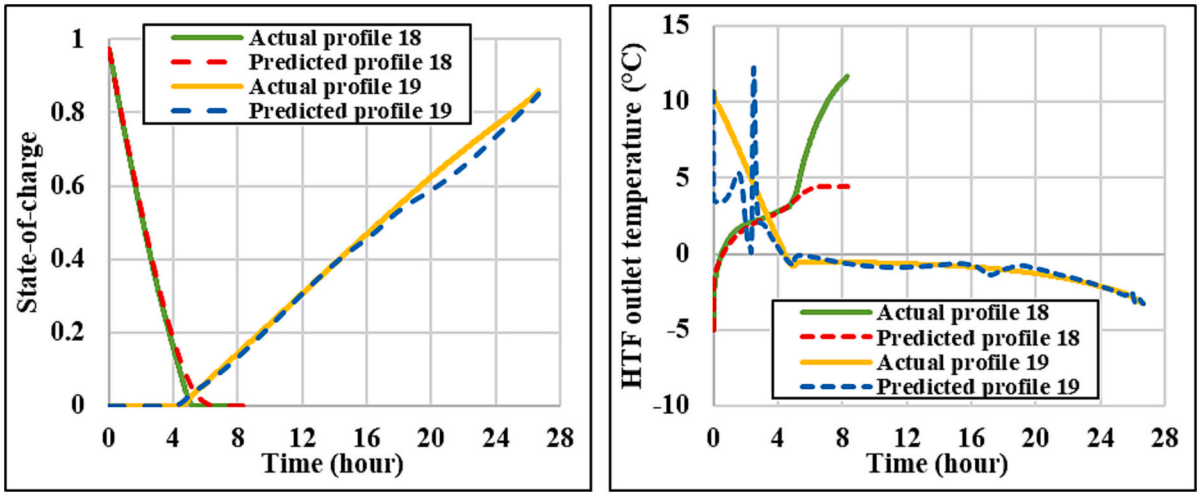

Fig. 17. *SoC* and T_o predictions by the NARX model with 2 ANNs (Case 176 in Table A3).

required to accurately predict the thermodynamics of phase transformation. Larger datasets may be also required to train the NARX model to a high accuracy.

Although the NARX model presented in this paper was developed for an ice tank, the methodology could be extended to predict the operation of other types of energy storage systems. However, modelling an LHTES unit for heating applications will require changes in the training and testing data containing the SoC values. For instance, the definition of SoC will be different from that discussed in Section 2. In a heating system, an SoC value of 0 will refer to a completely solidified PCM (representing a fully discharged TES unit), whereas a value of 1 will indicate a completely melted PCM (i.e. a fully charged TES unit). Additionally, suitable ranges of the HTF conditions (particularly the mass flow rate and input temperature) must be adopted. All these considerations may require modifications in the physics-informed connections among the ANNs within the NARX model for segregating different heating-cooling zones based on the modified SoC definition.

The previous limitations have been tackled by open-sourcing the developed NARX code so that users can re-develop new models with training data pertaining to any other energy storage capacity or for thermal stores used in heating applications. This will also enable users to create NARX models for LHTES units with other PCMs apart from a mixture of water-ice. For further information on how to use the NARX model and the type of problems it can help solving following suitable modifications of the code, the reader is referred to Appendix B. This may help the interested user to adapt the provided supplementary material accompanying this paper to their own applications.

For large-scale cooling networks that may require large capacity water-ice TES systems, multiple units of the TES tank investigated in this paper can be deployed for a parallel operation. In such a scenario, the presented NARX model may be implemented to monitor the operation of each such parallel TES unit.

The investigated NARX model is able to estimate values of SoC and T_o with a good accuracy in the occasional intervals of sensible heat and sensible cooling in the test profiles. Such a performance is sufficient for an ice tank. However, a greater emphasis must be placed on the physics-based and subsequent data-driven modelling aspects if the TES unit to be assessed is to be operated majorly in the sensible heat-cooling mode rather than in the phase transition mode. An example of such a TES system is a hot water tank employed for hot water provision and space heating. In this case, phenomena such as thermal stratification and convective currents may become significant as the mode of operation shifts majorly to sensible heat. It is thus recommended to use the presented model for estimating the output parameters of the LHTES unit operating in the phase-transition mode for which the practical storage unit and the computational models were originally designed and developed.

Similarly, the presented NARX architecture could be extended for predicting the operation of other types of energy storage systems such as large electric battery packs. This would require to identify the operating conditions and key variables affecting the performance of the battery. In addition to SoC, the state-of-health of each electric battery may be a relevant parameter affecting performance that must be monitored, which would add further complexity to the NARX model. While promising and of arguably a high research and industrial value, extending the work presented in this paper to other types of energy storage systems requires further comprehensive analysis which falls beyond the scope of this paper. These are nonetheless interesting avenues for continued research.

The methodology and tool based on a NARX architecture presented in this paper have the potential for practical deployment. For instance, other AI mechanisms for estimating SoC and state-of-health of electrical batteries have already been tested and deployed commercially [57,58]. This demonstrates industrial interest on the tools and provides supporting evidence of their viability for adoption in a practical thermal system.

4. Conclusions

LHTES units are important components supporting the operation of thermal systems such as district heating and district cooling networks. Managing the state of the thermal store is only possible if the SoC of the unit is known, although this may lead to high instrumentation costs and demanding technical specifications. To overcome these issues, this paper presented an AI model with a NARX architecture for predicting the operating conditions of a water-ice LHTES unit for cooling systems. The presented NARX model is 86% faster than a physics-based model and conducive to minimising experimental interventions for estimating the SoC and the outlet temperature of the HTF (T_o) of the LHTES unit. This characteristic makes the NARX model ideal for deployment in scenarios where retrieving output information is either computationally intensive or requires expensive instrumentation.

Upon being trained with data obtained from the simulations of a physics-based model, the NARX model accurately estimates unseen test data obtained from both the physics-based model and the real TES tank. The NARX model achieves average values of $R^2_{SoC} = 0.9943$ and $R^2_{T_o} = 0.9842$, with RMSE values of 1.73% for SoC and 0.3161°C for T_o over testing profiles obtained from the physics-based model and experimental data. In particular, the AI model results in average $R^2_{SoC} = 0.99$ and $R^2_{T_o} = 0.9774$ and values of RMSE of 2.95% for SoC and 0.4829°C for T_o with unseen experimental datasets, even when the NARX model was trained on data from the physics-based model. These results demonstrate the efficacy of the NARX model for possible deployment in the monitoring and controlling of a real-time operation of a TES unit.

The overall accuracy of the NARX model was improved by segregating the predictive tasks among different ANNs within the model according to the highly non-linear phenomena characterising the LHTES unit. This enabled the model to generate accurate SoC prediction profiles from different initial states of the storage medium (i.e. considering initial SoC values ranging between 0 and 1 inclusive). This demonstrates how embedding simple physics-based principles into the data-driven model could lead to more efficient data utilisation than end-to-end fully surrogate modelling. This further shows that not only the quantity of data for AI models is important, but also the way such data is utilised when developing the model matters greatly. For the LHTES unit under investigation, sensible heat and latent heat data, which have distinguishing underlying physics, act as noise to each other in the combined dataset. Thus, mixing these data profiles affects the prediction accuracy.

The NARX model and the numerical and experimental training-testing datasets have been open-sourced to support the scientific community given the limited availability of such models. Users can utilise the provided open-source NARX model to develop their own LHTES models with different capacities and storage media or create their own predictive models beyond the periphery of LHTES units and energy systems. This way, the methodology presented in this paper could be extended to latent heat thermal stores for heating applications, sensible heat units such as hot water tanks, and for monitoring the state of electrical energy storage systems such as large battery packs. These systems may have diverse underlying physics, which may influence the selection of parameters that need to be considered as input and output of prediction models.

CRediT authorship contribution statement

Pranaynil Saikia: Writing – review & editing, Writing – original draft, Visualization, Validation, Software, Methodology, Investigation, Formal analysis, Data curation, Conceptualization. **Héctor Bastida:** Writing – review & editing, Writing – original draft, Visualization, Validation, Software, Investigation, Data curation. **Carlos E. Ugalde-Loo:** Writing – review & editing, Writing – original draft, Supervision, Resources, Project administration, Investigation, Funding acquisition, Formal analysis.

Declaration of competing interest

The authors declare that they have no known competing financial interests or personal relationships that could have appeared to influence the work reported in this paper.

Data availability

The AI NARX model developed for this paper along with the relevant datasets have been made available as supplementary material. The same is also made available in the Cardiff University data catalogue at http://doi.org/10.17035/d.2024.0305908711.

Acknowledgement

The work presented in this paper was supported by the Engineering and Physical Sciences Research Council (EPSRC), UK Research and Innovation (UKRI), through the projects 'Flexibility from Cooling and Storage (Flex-Cool-Store)', Grant EP/V042505/1, and 'Multi-energy Control of Cyber-Physical Urban Energy Systems (MC2)', Grant EP/T021969/1.

Appendix A. TOPSIS analysis and results for determining relative suitability of different configurations of the NARX model

Table A1
Performance data of selected NARX configurations.

Case no.	Design parameters								Initial data from NARX model			
	ANN-1 neurons		ANN-4 neurons		Random state	ANN-1		ANN-4		Criteria 1 ($RMSE_{SoC}$)	Criteria 2 ($RMSE_{To}$) °C	Criteria 3 (R^2_{SoC})	Criteria 4 (R^2_{To})
	Hidden layer 1	Hidden layer 2	Hidden layer 1	Hidden layer 2		Activation function	Solver	Activation function	Solver				
32	4	14	6	15	73	logistic	adam	tanh	adam	0.01851	0.36315	0.99406	0.98020
41	3	13	8	5	244	logistic	adam	tanh	adam	0.02000	0.35667	0.99307	0.98137
55	3	8	9	14	220	tanh	adam	tanh	adam	0.01811	0.34989	0.99438	0.98158
56	4	6	10	14	70	logistic	adam	tanh	adam	0.01849	0.36420	0.99419	0.98130
69	11	7	15	14	52	logistic	adam	tanh	adam	0.02027	0.36602	0.99307	0.98108
73	4	12	6	8	228	logistic	adam	tanh	adam	0.01941	0.35012	0.99338	0.98254
82	11	4	9	9	141	tanh	adam	tanh	adam	0.01732	0.31609	0.99430	0.98416
101	12	7	14	6	66	tanh	adam	tanh	adam	0.02181	0.34702	0.99070	0.98135
110	5	4	12	4	250	logistic	adam	tanh	adam	0.02003	0.37137	0.99341	0.98060
130	3	15	6	8	213	tanh	adam	tanh	adam	0.01833	0.34758	0.99408	0.98185
160	14	10	13	12	6	relu	adam	tanh	adam	0.02512	0.37607	0.98830	0.98048
167	15	3	15	8	113	logistic	adam	tanh	adam	0.02282	0.37587	0.99115	0.98049
195	15	11	14	5	171	logistic	adam	tanh	adam	0.01910	0.35843	0.99339	0.98096
201	6	6	11	11	129	tanh	adam	tanh	adam	0.02025	0.35310	0.99282	0.98088
212	9	12	7	5	3	logistic	adam	tanh	adam	0.01938	0.37633	0.99361	0.98014
218	3	4	9	12	117	tanh	adam	tanh	adam	0.01954	0.32760	0.99285	0.98379
226	4	10	11	9	52	logistic	adam	tanh	adam	0.02077	0.36301	0.99279	0.98143
230	4	14	13	4	184	logistic	adam	tanh	adam	0.01854	0.34465	0.99421	0.98290
231	13	12	3	15	249	logistic	adam	tanh	adam	0.02023	0.36655	0.99247	0.98049
252	15	13	15	12	20	logistic	adam	tanh	adam	0.02232	0.37763	0.99164	0.98001
255	11	13	8	5	106	logistic	adam	tanh	adam	0.01998	0.37568	0.99316	0.98059
289	11	4	6	14	103	logistic	adam	tanh	adam	0.02064	0.34899	0.99185	0.98199
293	5	7	11	9	38	tanh	adam	tanh	adam	0.01838	0.33406	0.99323	0.98335

Table A2
Results of TOPSIS for determining the relative suitability of the filtered NARX configurations.

Case no.	Weight normalised data matrix				TOPSIS output			
	Criteria 1 ($RMSE_{SoC}$) °C	Criteria 2 ($RMSE_{To}$) °C	Criteria 3 (R^2_{SoC})	Criteria 4 (R^2_{To})	Euclidian distance from ideal solution (S+)	Euclidian distance from anti-ideal solution (S-)	Performance scores (S-) /[(S+) + (S-)]	Rank
32	0.15003	0.04674	4.3190E-05	3.0771E-05	1.1430E-02	5.3590E-02	0.82421	7
41	0.16212	0.04591	4.3147E-05	3.0808E-05	2.2401E-02	4.1554E-02	0.64974	12
55	0.14678	0.04503	4.3204E-05	3.0815E-05	7.7773E-03	5.6916E-02	0.87978	2
56	0.14982	0.04688	4.3196E-05	3.0806E-05	1.1330E-02	5.3791E-02	0.82602	6
69	0.16423	0.04711	4.3148E-05	3.0799E-05	2.4747E-02	3.9381E-02	0.61410	17
73	0.15729	0.04506	4.3161E-05	3.0845E-05	1.7513E-02	4.6429E-02	0.72611	9
82	0.14033	0.04068	4.3201E-05	3.0896E-05	3.6193E-09	6.3745E-02	1.00000	1
101	0.17676	0.04466	4.3044E-05	3.0807E-05	3.6646E-02	2.7109E-02	0.42520	20
110	0.16230	0.04780	4.3162E-05	3.0784E-05	2.3085E-02	4.1297E-02	0.64144	14
130	0.14851	0.04474	4.3191E-05	3.0823E-05	9.1247E-03	5.5211E-02	0.85817	4
160	0.20358	0.04840	4.2940E-05	3.0780E-05	6.3720E-02	2.0093E-04	0.00314	23
167	0.18494	0.04838	4.3064E-05	3.0780E-05	4.5265E-02	1.8646E-02	0.29175	22
195	0.15476	0.04613	4.3161E-05	3.0795E-05	1.5424E-02	4.8884E-02	0.76016	8
201	0.16411	0.04545	4.3137E-05	3.0792E-05	2.4246E-02	3.9604E-02	0.62027	15
212	0.15706	0.04844	4.3171E-05	3.0769E-05	1.8436E-02	4.6524E-02	0.71619	11
218	0.15834	0.04216	4.3138E-05	3.0884E-05	1.8068E-02	4.5699E-02	0.71666	10
226	0.16830	0.04672	4.3135E-05	3.0810E-05	2.8611E-02	3.5335E-02	0.55257	19
230	0.15027	0.04436	4.3197E-05	3.0856E-05	1.0590E-02	5.3488E-02	0.83473	5

(*continued on next page*)

Table A2 (*continued*)

Case no.	Weight normalised data matrix				TOPSIS output			
	Criteria 1 ($RMSE_{SoC}$) °C	Criteria 2 ($RMSE_{To}$) °C	Criteria 3 (R^2_{SoC})	Criteria 4 (R^2_{To})	Euclidian distance from ideal solution (S+)	Euclidian distance from anti-ideal solution (S-)	Performance scores (S-) /[(S+) + (S-)]	Rank
231	0.16398	0.04718	4.3121E-05	3.0780E-05	2.4520E-02	3.9632E-02	0.61778	16
252	0.18084	0.04860	4.3085E-05	3.0765E-05	4.1277E-02	2.2741E-02	0.35523	21
255	0.16192	0.04835	4.3151E-05	3.0784E-05	2.2907E-02	4.1666E-02	0.64525	13
289	0.16724	0.04492	4.3094E-05	3.0828E-05	2.7240E-02	3.6528E-02	0.57283	18
293	0.14896	0.04300	4.3154E-05	3.0870E-05	8.9311E-03	5.4911E-02	0.86011	3
Ideal soln.:	0.14033	0.04068	4.3204E-05	3.0896E-05				
Anti-ideal soln:	0.20358	0.04860	4.2940E-05	3.0765E-05				

Table A3
Selected best performing configurations for NARX with 2 ANNs.

Case no.	NARX Design parameters									Performance metrics				Rank from TOPSIS
	ANN-1 neurons		ANN-4 neurons		Random state	ANN-1		ANN-4		$RMSE_{SoC}$	$RMSE_{To}$ (°C)	R^2_{SoC}	R^2_{To}	
	Hidden layer 1	Hidden layer 2	Hidden layer 1	Hidden layer 2		Activation function	Solver	Activation function	Solver					
21	13	15	17	4	142	relu	adam	tanh	adam	0.02740	1.31728	0.98568	0.73813	5
23	7	13	5	41	120	relu	adam	tanh	adam	0.03106	1.33254	0.98385	0.73062	9
25	13	13	38	5	24	tanh	adam	tanh	adam	0.02883	1.36255	0.98311	0.71869	7
42	12	11	12	5	26	tanh	adam	tanh	adam	0.02080	1.29332	0.98864	0.74101	4
52	4	3	5	6	196	tanh	adam	tanh	adam	0.04566	1.39038	0.95151	0.72122	12
128	3	13	7	18	131	tanh	adam	tanh	adam	0.03383	1.35223	0.97766	0.72391	10
152	6	9	7	4	106	tanh	adam	tanh	adam	0.01669	1.41203	0.99279	0.70143	1
153	5	10	37	3	105	tanh	adam	tanh	adam	0.02811	1.41278	0.98488	0.70996	6
176	13	7	45	34	218	relu	adam	tanh	adam	0.01936	1.40913	0.98985	0.70531	2
200	11	11	30	10	86	relu	adam	tanh	adam	0.01990	1.38731	0.99041	0.70991	3
292	5	7	4	14	39	tanh	adam	tanh	adam	0.02931	1.28739	0.97683	0.75229	8
294	10	7	28	3	114	logistic	adam	tanh	adam	0.03594	1.37299	0.97677	0.70461	11
300	11	4	9	9	141	tanh	adam	tanh	adam	0.05948	1.94108	0.85985	0.26583	13

Appendix B. Further considerations on the open-source tool

This appendix provides additional information to guide the interested readers in incorporating the NARX-based AI tool to their own systems. It also gives some further insight on the specific application it addresses in its present form and how to customise it to consider other attributes in a TES tank.

B.1. Development environment of the NARX model

The development environment of the model was Python (version 3.10.11) in Jupyter Notebook IDE (version 6.4.10). The Python library dependencies briefly discussed below are considered.

1. math: used for calculating the square root of numbers.
2. numpy: used for creating arrays and performing array operations.
3. matplotlib: used for plotting the profiles of actual and predicted SoC and outlet temperature of the HTF.
4. pandas: used for reading and writing input/output data files.
5. sklearn: used for pre-processing input datasets, creating ANN models, and computing the RMSE.
6. time: used for assessing the time required to make predictions by the AI model.
7. tensorflow_addons: used for calculating R^2 values of predictions.
8. random: used for fixing a random seed to facilitate reproducibility of results.

B.2. Guidance on using the NARX model

The following steps provide a high-level guidance to use the NARX model:

1. Defining the *predict* function.
   a. The *predict* function takes as input a dataset and 4 ANNs (mdl, mdl2, mdl3, mdl4). Specific information on the ANNs was provided in Section 3.1. The ANN denoted as mdl is used to predict a change in SoC (represented as *dSoC* in the source code) during a phase transition of the PCM, whereas mdl2, mdl3, and mdl4 are used for the prediction of the outlet temperature of the HTF (represented as *OT* in the source code) during a phase transition, sensible heating-cooling of pure water, and sensible heating-cooling of pure ice.
   b. Pre-processing of the dataset including data sorting, scaling, and selection takes place inside the *predict* function. Therefore, there is no need to pre-process datasets before making any predictions.

c. The *predict* function returns the R^2 and RMSE values of the predictions along with the final predicted values of *SoC* and *OT*.
d. To activate the feedback mechanism for checking the accuracy of the model in long-term operations, set the "feedback_mechanism" variable to 'True'. Then, define the interval (in seconds) at which the feedback operation should be triggered to verify the prediction outputs against actual values. The actual values of SoC and OT for the same time-step should be available in the file "feedback.csv" (stored in the same folder as the NARX source code) for computing the absolute errors.

2. Training the model.
   a. The training dataset is created by stacking up (i.e. vertically sequencing) different profiles of the ice tank operations. Once the training dataset is loaded, the sorting, scaling, and selection operations are done on the training dataset. For further information, the reader is referred to the commented lines below the heading "training dataset input-output split" in the source code to see which data is used to train the different models for predictions of *dSoC* and *OT*.
   b. The 4 different ANNs (1 for *dSoC* and 3 for *OT* in different heating-cooling regimes) are then trained on the pre-processed training dataset.
3. Making predictions.
   a. Load a testing dataset from a CSV file. Follow the template of the test profiles provided along with the source code.
   b. Pass the loaded test dataset along with the 4 trained ANNs onto the *predict* function defined earlier to obtain the predicted profiles for *SoC* and *OT*.

In addition to the high-level descriptions mentioned in the steps above, a detailed explanation of each code block is provided through commented lines within the source code itself.

B.3. Guidance on customising the NARX model to consider different PCMs and sizes of TES units

As discussed in Section 3.5, the NARX model needs to be customised to make predictions for different types of PCM and sizes of TES tanks. These variations may likely require different profiles for inputs (i.e. mass flow rates and inlet temperatures of the HTF) and outputs (SoC and outlet temperature of the HTF) than those considered in this paper.

Users can create their own training and testing datasets for a different LHTES unit. While doing so, the same template of the CSV files for training (Training_dataset.csv) and testing (Test_profile_**.csv, where ** should be replaced with the test profile number) provided along this paper with the source code must be followed. In these files, the units of time, *mdot*, and *OT* are s, kg/s, and °C. *SoC* and *dSoC* have no units. The range of *SoC* is 0 to 1 where for a cooling application 0 represents a fully melted PCM (i.e. denoting a fully discharged tank) and 1 represents a fully solidified PCM (i.e. denoting a fully charged tank).

References

[1] Zhou Y. Transition towards carbon-neutral districts based on storage techniques and spatiotemporal energy sharing with electrification and hydrogenation. Renew Sustain Energy Rev 2022;162:112444. https://doi.org/10.1016/J.RSER.2022.112444.

[2] Cirocco L, Pudney P, Riahi S, Liddle R, Semsarilar H, Hudson J, et al. Thermal energy storage for industrial thermal loads and electricity demand side management. Energ Conver Manage 2022;270:116190. https://doi.org/10.1016/J.ENCONMAN.2022.116190.

[3] Wang Z, Mo X, Qin P, Zhao Z, Ouyang T. Multi-dimensional assessment and multi-objective optimization of electricity-cooling cogeneration system driven by marine diesel engine waste heat. J Clean Prod 2022;334:130187. https://doi.org/10.1016/J.JCLEPRO.2021.130187.

[4] Yang X, Sun D, Li J, Yu C, Deng Y, Yu B. Demonstration study on ground source heat pump heating system with solar thermal energy storage for greenhouse heating. J Energy Storage 2022;54:105298. https://doi.org/10.1016/J.EST.2022.105298.

[5] Hlimi M, Lebrouhi BE, Belcaid A, Lamrani B, Balli L, Ndukwu MC, et al. A numerical assessment of a latent heat storage system for district heating substations. J Energy Storage 2023;57:106210. https://doi.org/10.1016/J.EST.2022.106210.

[6] Chen Q, Wei W, Li N. Techno-economic control strategy optimization for water-source heat pump coupled with ice storage district cooling system. Int J Refrig 2022;138:148–58. https://doi.org/10.1016/J.IJREFRIG.2022.03.010.

[7] Bastida H, De la Cruz-Loredo I, Ugalde-Loo CE. Effective estimation of the state-of-charge of latent heat thermal energy storage for heating and cooling systems using non-linear state observers. Appl Energy 2023;331:120448. https://doi.org/10.1016/J.APENERGY.2022.120448.

[8] Ručevskis S, Akishin P, Korjakins A. Parametric analysis and design optimisation of PCM thermal energy storage system for space cooling of buildings. Energ Buildings 2020;224:110288. https://doi.org/10.1016/J.ENBUILD.2020.110288.

[9] Wang H, An C, Duan M, Su J. Transient thermal analysis of multilayer pipeline with phase change material. Appl Therm Eng 2020;165:114512. https://doi.org/10.1016/J.APPLTHERMALENG.2019.114512.

[10] Zhang C, Yu M, Fan Y, Zhang X, Zhao Y, Qiu L. Numerical study on heat transfer enhancement of PCM using three combined methods based on heat pipe. Energy 2020;195:116809. https://doi.org/10.1016/J.ENERGY.2019.116809.

[11] Ezzat Y, Abdel-Rehim AA. Numerical modelling of lauric acid phase change material using iterative and non-iterative time-advancement schemes. J Energy Storage 2022;53:105173. https://doi.org/10.1016/J.EST.2022.105173.

[12] What is Thermal Energy Storage? | Senmatic Sensors. https://www.senmatic.com/sensors/knowledge/thermal-energy-storage; 2022 (accessed August 15, 2023).

[13] Flow Rate Sensors for Measurement in Fluid Systems - Technical Articles. https://control.com/technical-articles/flow-rate-sensors-for-measurement-in-fluid-systems/; 2023 (accessed August 15, 2023).

[14] Electronic battery sensor. https://www.bosch-mobility.com/en/solutions/sensors/electronic-battery-sensor/; 2023 (accessed August 15, 2023).

[15] Chen D, Zhao Q, Zheng Y, Xu Y, Chen Y, Ni J, et al. Recent progress in lithium-ion battery safety monitoring based on fiber Bragg grating sensors. Sensors 2023;23:5609. https://doi.org/10.3390/S23125609.

[16] Morales Sandoval DA, De La Cruz Loredo I, Bastida H, Badman JJR, Ugalde-Loo CE. Design and verification of an effective state-of-charge estimator for thermal energy storage. IET Smart Grid 2021;4:202–14. https://doi.org/10.1049/STG2.12024.

[17] Dincer I, Rosen M. Thermal energy storage: Systems and applications. John Wiley & Sons; 2011.

[18] Shete KP, de Bruyn Kops SM, Kosanovic D, (Beka).. A first principles framework to predict the transient performance of latent heat thermal energy storage. J Energy Storage 2021;36:102388. https://doi.org/10.1016/J.EST.2021.102388.

[19] Steinmaurer G, Krupa M, Kefer P. Development of sensors for measuring the enthalpy of PCM storage systems. Energy Procedia 2014;48:440–6. https://doi.org/10.1016/J.EGYPRO.2014.02.052.

[20] Stovall TK. Calmac Ice Storage Test report. 1991. https://doi.org/10.2172/5210651.

[21] Bhamare DK, Saikia P, Rathod MK, Rakshit D, Banerjee J. A machine learning and deep learning based approach to predict the thermal performance of phase change material integrated building envelope. Build Environ 2021;199:107927. https://doi.org/10.1016/j.buildenv.2021.107927.

[22] Kanimozhi B, Ramesh Bapu BR, Pranesh V. Thermal energy storage system operating with phase change materials for solar water heating applications: DOE modelling. Appl Therm Eng 2017;123:614–24. https://doi.org/10.1016/J.APPLTHERMALENG.2017.05.122.

[23] Ermis K, Erek A, Dincer I. Heat transfer analysis of phase change process in a finned-tube thermal energy storage system using artificial neural network. Int J Heat Mass Transf 2007;50:3163–75. https://doi.org/10.1016/J.IJHEATMASSTRANSFER.2006.12.017.

[24] Xi Z, Wang R, Fu Y, Mi C. Accurate and reliable state of charge estimation of lithium ion batteries using time-delayed recurrent neural networks through the identification of overexcited neurons. Appl Energy 2022;305:117962. https://doi.org/10.1016/J.APENERGY.2021.117962.

[25] Chen Z, Zhao H, Zhang Y, Shen S, Shen J, Liu Y. State of health estimation for lithium-ion batteries based on temperature prediction and gated recurrent unit neural network. J Power Sources 2022;521:230892. https://doi.org/10.1016/J.JPOWSOUR.2021.230892.

[26] Benzaama MH, Menhoudj S, Mokhtari AM, Lachi M. Comparative study of the thermal performance of an earth air heat exchanger and seasonal storage systems: experimental validation of artificial neural networks model. J Energy Storage 2022;53:105177. https://doi.org/10.1016/J.EST.2022.105177.

[27] Song Y, Cai C, Ma D, Li C. Modelling and forecasting high-frequency data with jumps based on a hybrid nonparametric regression and LSTM model. Expert Syst Appl 2024;237:121527. https://doi.org/10.1016/J.ESWA.2023.121527.
[28] Scapino L, Zondag HA, Diriken J, Rindt CCM, Van Bael J, Sciacovelli A. Modeling the performance of a sorption thermal energy storage reactor using artificial neural networks. Appl Energy 2019;253:113525. https://doi.org/10.1016/J.APENERGY.2019.113525.
[29] Baker D, Asher Z, Bradley T. Investigation of vehicle speed prediction from neural network fit of real world driving data for improved engine on/off control of the EcoCAR3 hybrid Camaro. SAE Tech Pap 2017. https://doi.org/10.4271/2017-01-1262. 2017-March.
[30] Ren G, Chuttar A, Banerjee D. Exploring efficacy of machine learning (artificial neural networks) for enhancing reliability of thermal energy storage platforms utilizing phase change materials. Int J Heat Mass Transf 2022;189:122628. https://doi.org/10.1016/J.IJHEATMASSTRANSFER.2022.122628.
[31] Muthya Goud V, Sudhakar DR. A comprehensive investigation and artificial neural network modeling of shape stabilized composite phase change material for solar thermal energy storage. J Energy Storage 2022;48:103992. https://doi.org/10.1016/J.EST.2022.103992.
[32] Eldokaishi AO, Abdelsalam MY, Kamal MM, Abotaleb HA. Modeling of water-PCM solar thermal storage system for domestic hot water application using artificial neural networks. Appl Therm Eng 2022;204:118009. https://doi.org/10.1016/J.APPLTHERMALENG.2021.118009.
[33] Keras: the Python deep learning API. https://keras.io/; 2023 (accessed February 20, 2023).
[34] Neural network - Example for NARX in python - both training and prediction - Stack Overflow. https://stackoverflow.com/questions/59277119/example-for-narx-in-python-both-training-and-prediction; 2023 (accessed February 20, 2023).
[35] Python - NARX implementation using keras - Stack Overflow. https://stackoverflow.com/questions/53087669/narx-implementation-using-keras; 2023 (accessed February 20, 2023).
[36] PyNeurGen. https://pyneurgen.sourceforge.net/recurrent.html; 2023 (accessed February 20, 2023).
[37] Models module — fireTS 1.0.1 documentation. https://firets.readthedocs.io/en/latest/models.html; 2023 (accessed February 20, 2023).
[38] ARX Time Series Model. https://apmonitor.com/wiki/index.php/Apps/ARXTimeSeries; 2023 (accessed February 20, 2023).
[39] Fraicheur de Paris | District cooling network. https://www.fraicheurdeparis.fr/reseau-de-froid-urbain#cooling_network_map; 2023 (accessed November 23, 2023).
[40] Brok N, Green T, Heerup C, Oren SS, Madsen H. Optimal operation of an ice-tank for a supermarket refrigeration system. Control Eng Pract 2022;119:104973. https://doi.org/10.1016/J.CONENGPRAC.2021.104973.
[41] CALMAC. IceBank Energy Storage Model C. http://www.calmac.com/icebank-energy-storage-model-c?showSpecs; 2023 (accessed February 20, 2023).
[42] Bastida H, Ugalde-Loo CE, Abeysekera M, Jenkins N. Dynamic modelling of ice-based thermal energy storage for cooling applications. IET Energy Syst Integr 2022;4:317–34. https://doi.org/10.1049/ESI2.12061.
[43] Drees KH, Braun JE. Modeling of area-constrained ice storage tanks. HVAC R Res 1995;1:143–58. https://doi.org/10.1080/10789669.1995.10391315.
[44] López-Navarro A, Biosca-Taronger J, Torregrosa-Jaime B, Corberán JM, Bote-García JL, Payá J. Experimental investigations on the influence of ice floating in an internal melt ice-on-coil tank. Energ Buildings 2013;57:20–5. https://doi.org/10.1016/J.ENBUILD.2012.10.040.
[45] López-Navarro A, Biosca-Taronger J, Torregrosa-Jaime B, Martínez-Galván I, Corberán JM, Esteban-Matías JC, et al. Experimental investigation of the temperatures and performance of a commercial ice-storage tank. Int J Refrig 2013;36:1310–8. https://doi.org/10.1016/J.IJREFRIG.2012.09.008.
[46] Aggarwal CC. Neural networks and deep learning : A textbook. Springer; 2018.
[47] Buevich A, Sergeev A, Shichkin A, Baglaeva E. A two-step combined algorithm based on NARX neural network and the subsequent prediction of the residues improves prediction accuracy of the greenhouse gases concentrations. Neural Comput Applic 2021;33:1547–57. https://doi.org/10.1007/S00521-020-04995-4/FIGURES/8.
[48] Sharma A, Tyagi VV, Chen CR, Buddhi D. Review on thermal energy storage with phase change materials and applications. Renew Sustain Energy Rev 2009;13:318–45. https://doi.org/10.1016/J.RSER.2007.10.005.
[49] Barz T, Seliger D, Marx K, Sommer A, Walter SF, Bock HG, et al. State and state of charge estimation for a latent heat storage. Control Eng Pract 2018;72:151–66. https://doi.org/10.1016/J.CONENGPRAC.2017.11.006.
[50] sklearn.neural_network.MLPRegressor — scikit-learn 1.2.1 documentation. https://scikit-learn.org/stable/modules/generated/sklearn.neural_network.MLPRegressor.html; 2023 (accessed February 20, 2023).
[51] Saikia P, Gaurav Rakshit D. Designing a clean and efficient air conditioner with AI intervention to optimize energy-exergy interplay. Energy AI 2020:100029. https://doi.org/10.1016/j.egyai.2020.100029.
[52] Verma A, Saikia T, Saikia P, Rakshit D, Ugalde-Loo CE. Thermal performance analysis and experimental verification of lithium-ion batteries for electric vehicle applications through optimized inclined mini-channels. Appl Energy 2023;335:120743. https://doi.org/10.1016/J.APENERGY.2023.120743.
[53] Saikia P, Rakshit D, Narayanaswamy R, Wang F, Udayraj.. Energy performance and indoor airflow analysis of a healthcare ward designed with resource conservation objectives. J Build Eng 2021;44:103296. https://doi.org/10.1016/J.JOBE.2021.103296.
[54] Das D, Sharma RK, Saikia P, Rakshit D. An integrated entropy-based multi-attribute decision-making model for phase change material selection and passive thermal management. Decis Anal J 2021;1:100011. https://doi.org/10.1016/J.DAJOUR.2021.100011.
[55] Zhang Y. TOPSIS method based on entropy weight for supplier evaluation of power grid enterprise. Atlantis Press; 2015. p. 334–7. https://doi.org/10.2991/ermm-15.2015.88.
[56] Khalil HK. Nonlinear control. Essex, England: Pearson; 2015.
[57] AI-driven Battery Management System for Electric Vehicles. https://www.bluewind.it/site/wp-content/uploads/2018/11/BW20200406-WP-IBMS.pdf; 2020 (accessed August 15, 2023).
[58] AI-Powered Cloud-Connected Battery Management System for Electric Vehicles | NXP Semiconductors. https://www.nxp.com/company/about-nxp/ai-powered-cloud-connected-battery-management-system-for-electric-vehicles:NW-NXP-AI-POWERED-CLOUD-CONNECTED-BATTERY; 2022 (accessed August 15, 2023).